SANDIA REPORT

SAND2016-0224
Unlimited Release
Printed January 2016

Fire Intensity Data for Validation of the Radiative Transfer Equation

Thomas Blanchat and Dann Jernigan

Prepared by
Sandia National Laboratories
Albuquerque, New Mexico 87185 and Livermore, California 94550

Sandia National Laboratories is a multi-program laboratory managed and operated by Sandia Corporation, a wholly owned subsidiary of Lockheed Martin Corporation, for the U.S. Department of Energy's National Nuclear Security Administration under contract DE-AC04-94AL85000.

Issued by Sandia National Laboratories, operated for the United States Department of Energy by Sandia Corporation.

Available to DOE and DOE contractors from
U.S. Department of Energy
Office of Scientific and Technical Information
P.O. Box 62
Oak Ridge, TN 37831

Telephone: (865) 576-8401
Facsimile: (865) 576-5728
E-Mail: reports@adonis.osti.gov
Online ordering: http://www.osti.gov/bridge

Available to the public from
U.S. Department of Commerce
National Technical Information Service
5285 Port Royal Rd.
Springfield, VA 22161

Telephone: (800) 553-6847
Facsimile: (703) 605-6900
E-Mail: orders@ntis.fedworld.gov
Online order: http://www.ntis.gov/help/ordermethods.asp?loc=7-4-0#online

SAND20**-****
Unlimited Release
Printed *** ****

Fire Intensity Data for Validation of the Radiative Transfer Equation

Thomas K. Blanchat and Dann Jernigan

Fire Science and technology Department
Sandia National Laboratories
PO Box 5800
Albuquerque, NM 87185

Abstract

A set of experiments and test data are outlined in this report that provides radiation intensity data for the validation of models for the radiative transfer equation. The experiments were performed with lightly-sooting liquid hydrocarbon fuels that yielded fully turbulent fires 2 m diameter). In addition, supplemental measurements of air flow and temperature, fuel temperature and burn rate, and flame surface emissive power, wall heat, and flame height and width provide a complete set of boundary condition data needed for validation of models used in fire simulations.

CONTENTS

FIGURES

TABLES

ACKNOWLEDGEMENT

The author acknowledges and thanks the following individuals; Allen Ricks and Sean Kearney who coauthored Appendix A and also contributed to the discussion on the intensity measurement results.

As always, these experiments could not have been performed without the support of the extremely capable technologists in the Fire and Aerosol Sciences Department and the TMSS support group who assembled the hardware and ran the tests. Especially notable is Dann Jernigan who led the setup and conducted every experiment with help from Martin Sanchez, Ciro Ramirez, and Jesse Fowler. In addition, Ciro Ramirez developed the macros to analyze the extensive video datasets to determine flame height and widths. The work reported here could not have been done without them.

Lastly, I want to thank those who performed the peer-review of this report, John Hewson and Sean Kearney.

Financial support for this project was provided by the Weapon System Engineering Assessment Technology (WSEAT) Campaign 6 and the Engineering Sciences Research Foundation (ESRF). The authors appreciate management's continued support for diagnostics development and validation quality data sets. Finally, we note that Engineering Sciences has a clear commitment to science in support of our weapons programs and is committed to supporting the research community through publication of its data sets where appropriate.

NOMENCLATURE

CARS	coherent anti-Stokes Raman scattering
LII	laser induced incandescence
CGA	Combustion Gas Analyzer
DAS	data acquisition system
FRH	FLAME/Radiant Heat
HP	Hewlett-Packard
MUX	more multiplexer unit
NI	National Instruments
SNL	Sandia National Laboratories
TTC	Thermal Test Complex

1. BACKGROUND AND MOTIVATION

Radiative emission from even the largest fires is a primarily local phenomenon, occurring at length scales dictated by the size of individual flames within the larger fire plume, and it is prohibitively expensive to resolve in practical fire-simulation models. Moreover, soot volume fraction, unlike many other scalar properties, is not well correlated with the mixture fraction in flamelet-type approaches, rendering soot modeling in turbulent fire environments even more challenging. Further development and refinement of subgrid radiation source-term models, therefore, requires highly spatially and temporally resolved temperature and soot data, as the correlation of these two scalars is needed to describe the generation of soot radiation in large fires.

The equation of radiative transfer (discussed in detail in Appendix A) equates the net radiation to an object as the sum of the emitted and absorbed radiation along the line of sight. The test plan by Kearney et al [2010] describes all of the measurements and experiments to provide data for validation of models for the radiative transfer equation, shown in one form below (that assumes the size of the soot particles is much less than the wavelength of the radiation so that scattering is negligible):

$$\frac{dI_\lambda}{ds} = \mu_\lambda I_{\lambda,b}(T) - \mu_\lambda I_\lambda \quad , \tag{1}$$

where I_λ is the radiative intensity at a point, *s,* along the direction of the ray of interest; $I_{\lambda,b}$ is the blackbody spectral intensity at *s,* where the local temperature is *T*; and μ_λ is the absorption coefficient. In this context, Eq. 1 simply states that the change in *I* along *s* is emission minus absorption.

A set of experiments and test data are outlined in this report that provides radiative intensity data for the above radiative transfer equation. The experiments were performed with lightly-sooting liquid hydrocarbon fuels that yielded fully turbulent fires (2 m diameter).

2. DESIGN OF EXPERIMENTS

The key test conditions for the nine tests are summarized in Table 1. Two fuel mixtures were selected. The first was a liquid fuel mixture of 72.4% methanol and 27.6% toluene, chosen because it a light to medium sooting fuel (to allow combined CARS/LII measurements) and it is also an azeotrope; a mixture of two or more liquids in such a ratio that its composition cannot be changed by simple distillation. When an azeotrope is boiled, the resulting vapor has the same ratio of constituents as the original mixture. The second mixture was a liquid fuel mixture of 90% methanol and 10% toluene (a light sooting fuel), chosen due to the possibility that the combined CARS/LII measurements (separate experiments to be performed later) would not be able to measure with the azeotrope fuel.

Eight experiments were performed, five with the azeotrope fuel and three with a Met90/Tol10 mix. For each fuel, intensity measurements (horizontal scans described later) were taken at three heights above the fuel surface (0.5 m, 1.0 m, and 1.5 m) and twenty horizontal positions (0.1 m apart). A repeat data set was taken for each test except

for the first test (T2). Typically, for each test, the fire was run in a constant level mode (continuous fuel feed), after waiting about ten minutes the first scan was started, each scan took about 10 minutes to complete, the spectrometer water-cooled viewing tube was pulled out of the fire, and the second scan was started.

Table 1 Test Summary

Name	Test Date	Fuel Mixture	Spectrometer Scan Height Above Pool (m)
T2	12/1/2010	Methanol72% / Toluene28%	0.5
T3	12/7/2010	Methanol72% / Toluene28%	0.5
T4	12/9/2010	Methanol90% / Toluene10%	0.5
T5	12/15/2010	Methanol72% / Toluene28%	1.0
T6	12/16/2010	Methanol72% / Toluene28%	1.0
T7	12/16/2010	Methanol90% / Toluene10%	1.0
T8	12/21/2010	Methanol90% / Toluene10%	1.5
T9	12/22/2010	Methanol72% / Toluene28%	1.5

Table 2 presents properties of the fuels and fire parameters assuming a 2 m diameter pool. Mixture rules (based on mole%) were used to estimate mixture properties. A fuel mixture of methanol80% / toluene20% is included for reference, in the event tests will be performed with this mixture at a later date.

Table 2 Fuel Properties

			Literature Values for Pure Fuels			Calculated Values for Fuel Mixtures (using mixture rules)	Calculated Values for Fuel Mixtures (using mixture rules)	Calculated Values for Fuel Mixtures (using mixture rules)
Properties	**Properties**	**Units**	**methyl alcohol**	**toluene**		**90.0% Methanol 10.0% Toluene**	**80.0% Methanol 20.0% Toluene**	**72.4% Methanol 27.6% Toluene**
Name	**Formula**	**-**	**CH_4O**	**C_7H_8**		**CH_4O/C_7H_8**	**CH_4O/C_7H_8**	**CH_4O/C_7H_8**
molecular weight	MW	-	32.1	92.1		34.5	37.3	39.7
Boiling point handbook	T_b	C	64.8	110.4		67	69	71
smoke point	l_s	m	0.281	0.005		0.100	0.100	0.100
heat of vaporization	hv	kJ/kg	1101.0	360.0		887	885	883
specific heat	c_p	kJ/kg K	2.37	1.67		1.99	2.09	2.16
heat of gasification	hg	kJ/kg	1272	520		1035	1043	1050
density	ρ	kg/m^3	791.4	866.9		695	759	814
heat of combustion	Δhc	kJ/kg	19718	41630		19210	22954	26173
heat of combustion (measured)	Δhc	kJ/kg						26080
carbon monoxide component	Δhc_{CO}	kJ/kg	12900	9000		10848	11333	11751
carbon dioxide component	Δhc_{CO2}	kJ/kg	14500	12100		12380	13140	13793
oxygen component	Δhc_{O2}	kJ/kg	13400	12900		11603	12490	13253
burning rate$_\infty$	max m"-dot	kg/m^2 s	0.015	0.075		0.019	0.026	0.033
incompleteness of combustion	χ_{ch}	-	0.95	0.67		0.80	0.84	0.87
radiant fraction	χ_r	-	0.14	0.4		0.15	0.18	0.22
smoke yield	ψ_s	g/g	0.002	0.178		0.018	0.037	0.053
Pan Diameter (m)	2.00				**Component**	**mole%**	**mole%**	**mole%**
Pan Area (m^2)	3.14				**Toluene**	0.041	0.087	0.127
					Methanol	0.959	0.913	0.873
					Component	**# mole**	**# mole**	**# mole**
References:					**Toluene**	0.941	1.882	2.597
Archies new SFPE tables					**Methanol**	22.223	19.754	17.877
SFPE ed. 2, Table 3-4.7								
SFPE ed. 2, Table C-2					**Component**	**mass%**	**mass%**	**mass%**
Industrial Fire Protection Engineering, Table 7.4					**Toluene**	0.109	0.215	0.295
SFPE ed. 2, Table 3-4.19					**Methanol**	0.891	0.785	0.705
Aviation Fuel Properties, Coordinating Research Council, Inc. 1988								
Distillation Range 177-266 C					**Component**	**Volume %**	**Volume %**	**Volume %**
kerosene	2m complex				**Toluene**	0.100	0.200	0.276
SFPE ed. 3, Table 3-4.10					**Methanol**	0.900	0.800	0.724
Galbraith Labs								

2.1 Test Procedures

The fire was ignited with a propane igniter and allowed to burn for approximately 5 minutes before taking data to avoid the initial transient phase of the fire. Fire durations ranged from 20-40 minutes. Filling of the fuel pool to maintain a constant fuel level was performed automatically throughout the test and the amount of fuel added was measured. Mean fuel regression rates are found from the time-averaged filling rates.

2.2 Data Acquisition

The data acquisition system (DAS) for all standard fire and fuel measurements and facility instrumentation consisted of a PC with a 16-bit data acquisition card connected to a National Instruments (NI) SCXI-1001 chassis. It has twelve NI SCXI-1102 cards with NI SCXI-1303 blocks for thermocouples (TCs) and four NI SCXI-1104 cards with NI SCXI-1300 blocks for analog signals. This provided the ability to increase either analog signals or TC signals. The data acquisition system can acquire temperature, heat flux, and pressure data. The integrity of all thermocouple channels was evaluated prior to the start of the experimental series with an Ectron thermocouple simulator, which inputs a controlled signal into each channel at the thermocouple device connection point and provides a check on the integrity of the channel hardware and software from that point to the final magnetic storage location. Data are sampled simultaneously for all channels, typically at 1000 Hz with an average value recorded at a rate of at least one sample per second, starting at least two minutes prior to the fuel ignition and continuing after burnout of the fire.

A formal checklist for conducting the test was created and used to record actions during the test event. The data from the instrumentation are organized via a Data Channel Summary Sheet and with sketches showing instrumentation location. This summary sheet contains a channel-by-channel listing of the instrumentation with details such as expected range, sampling rate, calibration date and source, instrument location, and the data sample rate. Post-test, all data are collected and converted to electronic format for purposes of archiving and dissemination.

3. FACILITY, INSTRUMENTATION, AND MEASUREMENTS

3.1 FRH Facility Description

The experiments were conducted in a controlled fire environment inside the FLAME/Radiant Heat (FRH) test cell in the Thermal Test Complex (TTC) at Sandia National Laboratories (SNL). The main test chamber of the FRH cell is cylindrical in shape, 60 ft (18 m) inner diameter with a height around the perimeter of 40 ft (12 m). The ceiling slopes upwards (~18º) from the perimeter walls to a height of 48 ft (15 m) over the center of the facility. A round hole at the top of the facility 16 ft (4.9 m) diameter transitions to a 10 ft by 12 ft (3.0 m by 3.7 m) chimney duct. The outer walls are made of steel channel sections and are filled with water that acts as a thermal sink during tests.

The ground level of FRH can be divided into three concentric sections. At the center of the facility is a fuel pan or gas burner. The facility can operate a gas burner (He, H_2, CH_4, etc.) or a liquid fuel pool (JP-8, methanol, etc.) up to 3 m in diameter. The test series discussed here used a 2 m diameter fuel pan. The second section is a steel spill plate, which extends to a diameter of 6 m. The floor of the outer section is made of a steel grating, through which air is supplied to the FRH chamber during fire experiments.

Figure 1 gives a cutaway view of the FLAME/Radiant Heat (FRH) test cell showing a pool fire at the ground level, pipes supplying air flow through the basement, the chimney, and instrumentation rooms outside the FRH chamber.

The air flow in the FRH chamber combines contributions due to the buoyancy-controlled fire and due to the forced flow of air through the facility. Eighteen supply pipes carry the air from the large diffuser in the center of the facility to the air ring along the outer circumference in the facility basement, where it then flows into the FRH cell at the floor grating (refer to Figure 1).

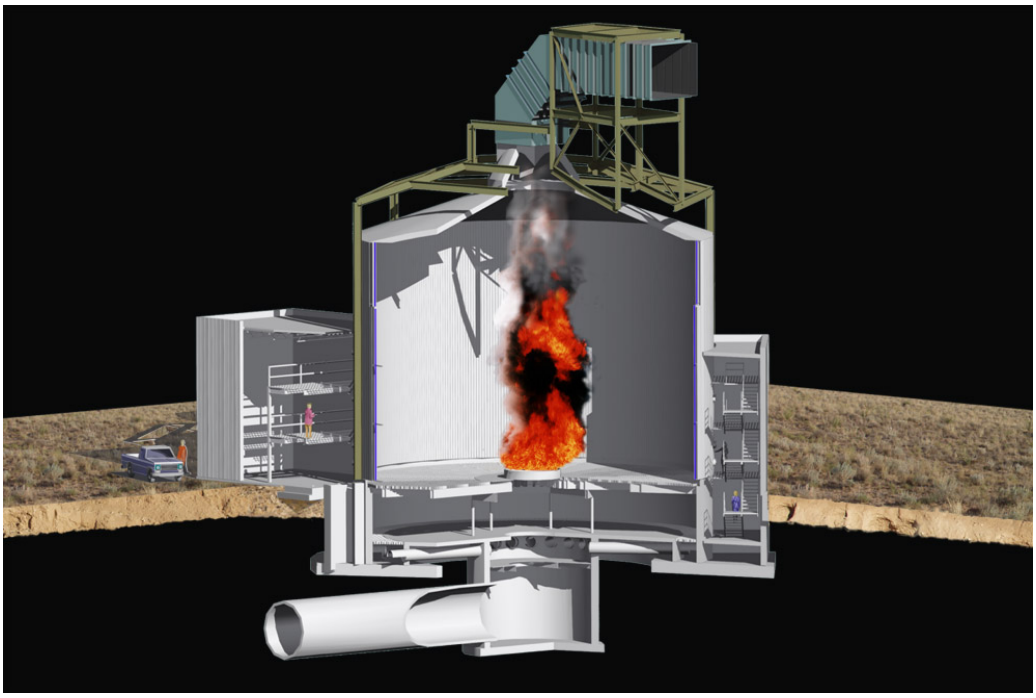

Figure 1 A cutaway view of the FRH facility.

3.2 Principal Measurement

3.2.1 Flame Internal Intensity versus Path Length

A horizontal, water-cooled, stainless steel tube (3 inch I.D., 120 inches long) was attached to the inlet port (sapphire window) of an imaging spectrometer (model ES-200, Spectraline, Inc., West Lafayette, IN) to obtain mid-infrared spectral radiation intensity measurements inside the fire.

The ES-200 (Figure 2) measures spectral radiation intensity at 390 Hz in the 1.3 to 4.8 micron wavelength range and each of the 256 pixels looks at a wavelength of 22 nm (note that each set of 236 pixel data is acquired in ~2.5 ms). This wavelength range accounts for 75% of the emitted radiation energy from a blackbody source at 1420 K, which is approximately the effective radiation temperature from a large hydrocarbon fuel fire as determined by Kearney [2001]. The acceptance angle of the spectrometer is ±0.27 degrees. The water-cooled viewing tube and spectrometer were mounted on a horizontal translator table to provide horizontal scans across the fuel pan and obtain intensity data at exact locations. The spectrometer was mounted outside the fire. A small flow of nitrogen through the spectrometer and tube was used to keep the optics clean and eliminate the contaminating effects of changes in gas composition within the pipe.

Figure 2 Spectraline ES200, laptop, and data acquisition system.

Table 3 provides the specifications for the ES-200. Radiation enters the inlet port of the ES 200 through a sapphire window mounted on the interface plate. It is then chopped by a tuning fork chopper oscillating at a specific frequency. The chopped radiation falls on a set of mirrors and off-axis parabolas that collimate the beam. The beam then passes through a set of calcium fluoride prisms that disperse it into its component wavelengths. The dispersed beam falls on another parabolic mirror that reflects it on to the detector array. The detector is an array of 256 Lead Selenide elements arranged in a linear fashion. These pixel elements respond to the incident radiation by producing an output current. The built-in multiplexer reads these currents at 1 MHz and provides it at the camera output. The proprietary drive circuit converts these currents to voltages, amplifies them and sends them to the data acquisition board. The Infraspec software reads the data acquisition board and writes the data to memory. The software then calculates the intensities corresponding to each voltage and plots it against the corresponding wavelength.

Table 3 ES-200 Technical Specifications

Imaging Spectrometer	
Detector	256 pixel PbSe array
Pixel size	33 x 100 microns
Nominal wavelength range	1.3 to 4.8 microns (7692 - 2083 cm^{-1})
Acceptance angle	+/- 0.27 degrees
Spectral resolution	0.014 microns (14 nanometers)
Accuracy	0.5 % of full range
Responsivity	6e8 volts/watt
Sensor dynamic range	> 2000: 1
Frame acquisition rate	4680 / 15840 Hz
Frame sampling rate	390 / 1320 Hz

The spectrometer was calibrated using a blackbody source with a 1 inch aperture (Infrared Systems Development Corporation, Model IR-301, SN3119K, 0-1200°C range) at the beginning of the experimental series. When referenced with calibrations obtained using a black body, the data provides the absolute values of radiation intensities recorded by the detector array.

Figure 3 and Figure 4 show the spectrometer, water-cooled viewing tube, and horizontal translation table mounted on an insulated steel uni-strut frame positioning system which traversed in the vertical direction to shift the spectrometer viewing location from a height of ~1.7 m above the pool surface to close to the fuel pool surface. The ~3 m long viewing tube allowed spectrometer measurements that completely spanned the 2 m diameter fuel pan.

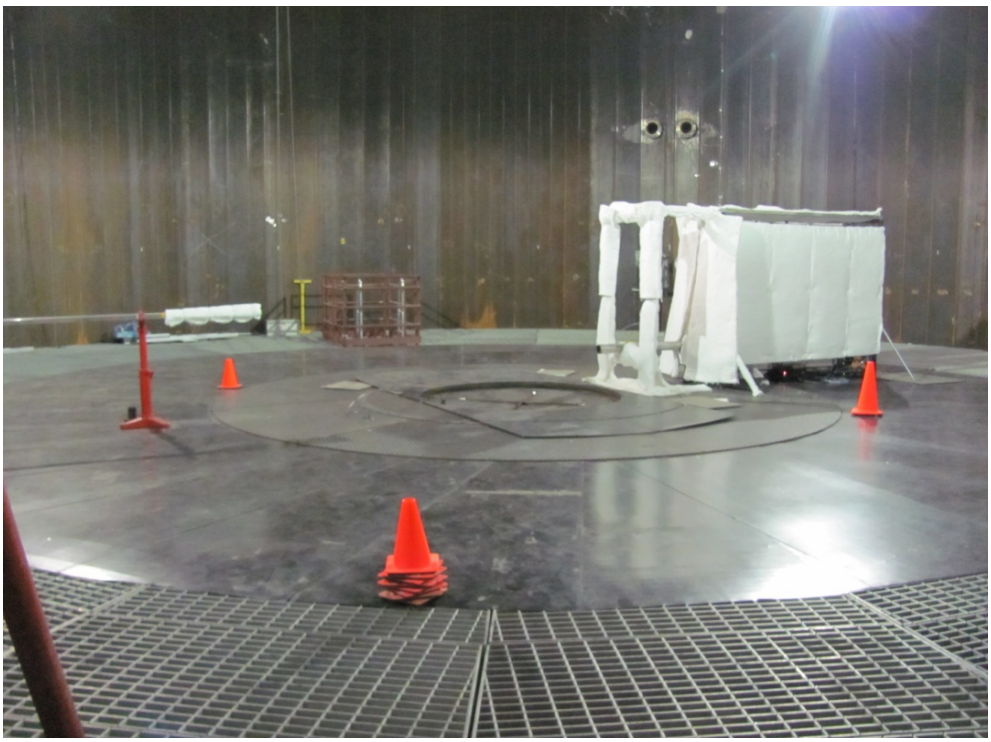

Figure 3 Spectrometer setup showing viewing tube exiting enclosure.

The horizontal translation table was fabricated using a Velmex BiSlide tandem mount (two slides mounted together from the side for strength) with a Vexta Type 34T1 Stepper motor. The motor was controlled via a standalone software package from Velmex. The slide had 76 inches of usable travel with a resolution of 0.1inch/revolution of the grooved rod (note that 5000 steps on the stepper motor yielded a horizontal translation of 1 inch).

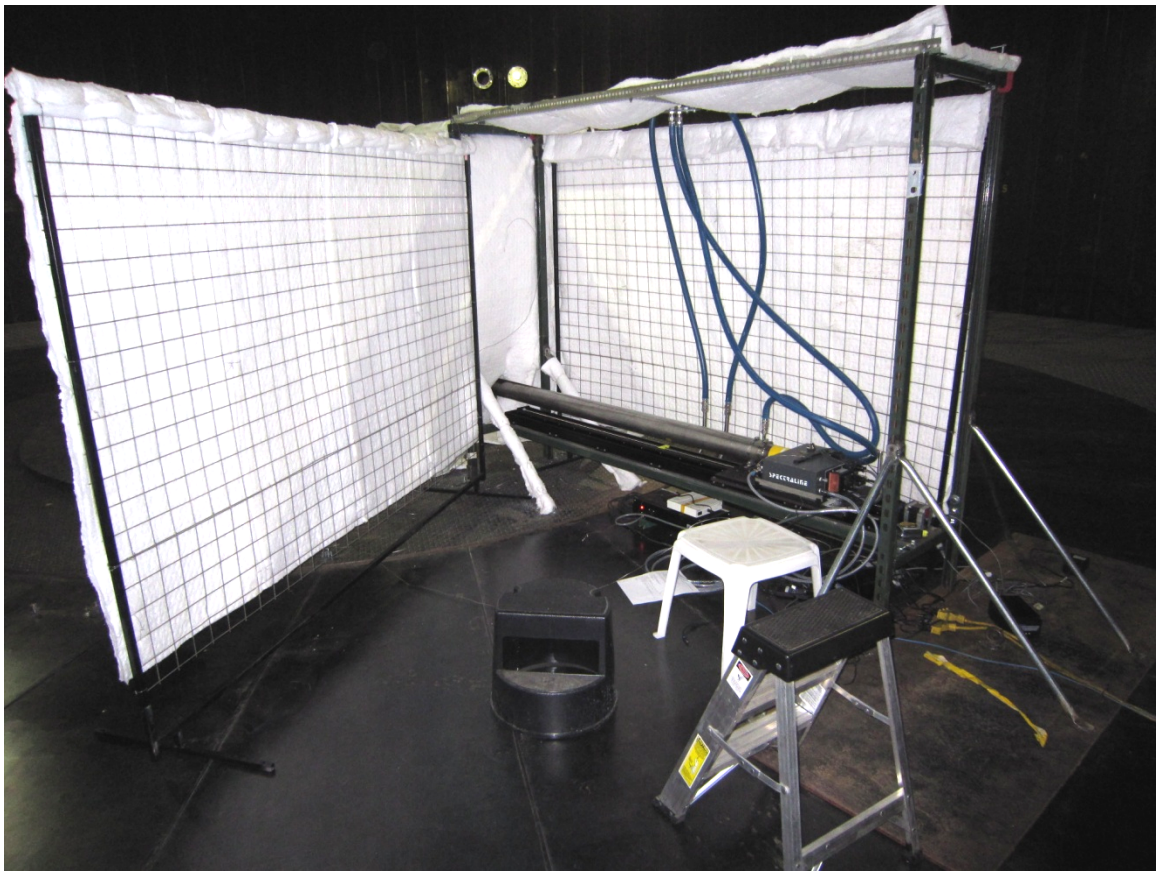

Figure 4 Spectrometer setup (looking inside enclosure).

The nitrogen purge gas flow rate was initially set to 5 LPM, based on a diffusion calculation to limit the flow of combustion gases (assumed all methanol in air, diffusion coefficient = 1.32e-5 m^2/s) into the cooled spectrometer tube to a distance of 1 inch. This gave a diffusion velocity of ~0.5 mm/s, approximately $1/10^{th}$ of the nitrogen purge gas velocity. However, it was noted that during T5 the first ~5 inches of the cooling tube interior was coated with a thin layer of soot; the purge flow was increased to 50 LPM with the result that very little soot was seen in later tests.

3.3 Supplemental and Boundary Condition Measurements

3.3.1 Flame topology (Height and Diameter) – Video and IR cameras

The average flame height was determined from visual data from two Canon XH A1 1080 High-Definition video camcorders mounted on the wall of the FRH test cell. One camcorder was mounted normally and one was mounted on its side to take advantage of the three 16:9 sensors (1440x1080 pixels, one for each color) to capture the long flame plume. Prior to the test each position within the camera frame was mapped to a height above the fuel surface at the centerline of the fire using a stadia board. The stadia board, shown in Figure 5, has calibrated marks at 0.1 m intervals, providing a resolution of 0.05 m (the right hand picture shows an overlay of the stadia board during a fire). The stadia board, actually a 12 m long ruler suspended from the ceiling, was moved adjacent to the FLAME wall during testing. The flame height analysis, described below, determined the median and average height of each fire.

Figure 5 Stadia board used in flame height calibration and analysis.

For each selected averaging period within a test, thirty seconds of video data (900 frames, starting at the beginning of the steady-state time period listed in Table 5) recorded during steady state "puffing" conditions (indicating fully turbulent conditions) were analyzed to determine the median and average flame heights. To automate the process, imaging analyses software (ImagePro®) was used to provide the average pixel intensity at each horizontal row of a 1/3 burner diameter wide vertical line drawn through the burner centerline (yellow lines shown in Figure 5).

It was necessary to determine the threshold intensity to be used for each test, which changed due to differences in flame color and camera settings. A Fortran routine was used to process the vertical line profile intensity of the 900 frame dataset, varying the threshold intensity from 0 to 255 and determining the average flame height at each intensity. As the threshold intensity increases, a sharp drop followed by a "knee" occurs at the flame top. As the threshold intensity increases, the estimated flame height gradually decreases as the line profile progresses further down into the flame. The actual intensity used in the analysis is chosen by inspection, within ~10 units of intensity below the knee. Figure 6 shows the vertical line profiles for all tests yielding the average height as a function of threshold intensity.

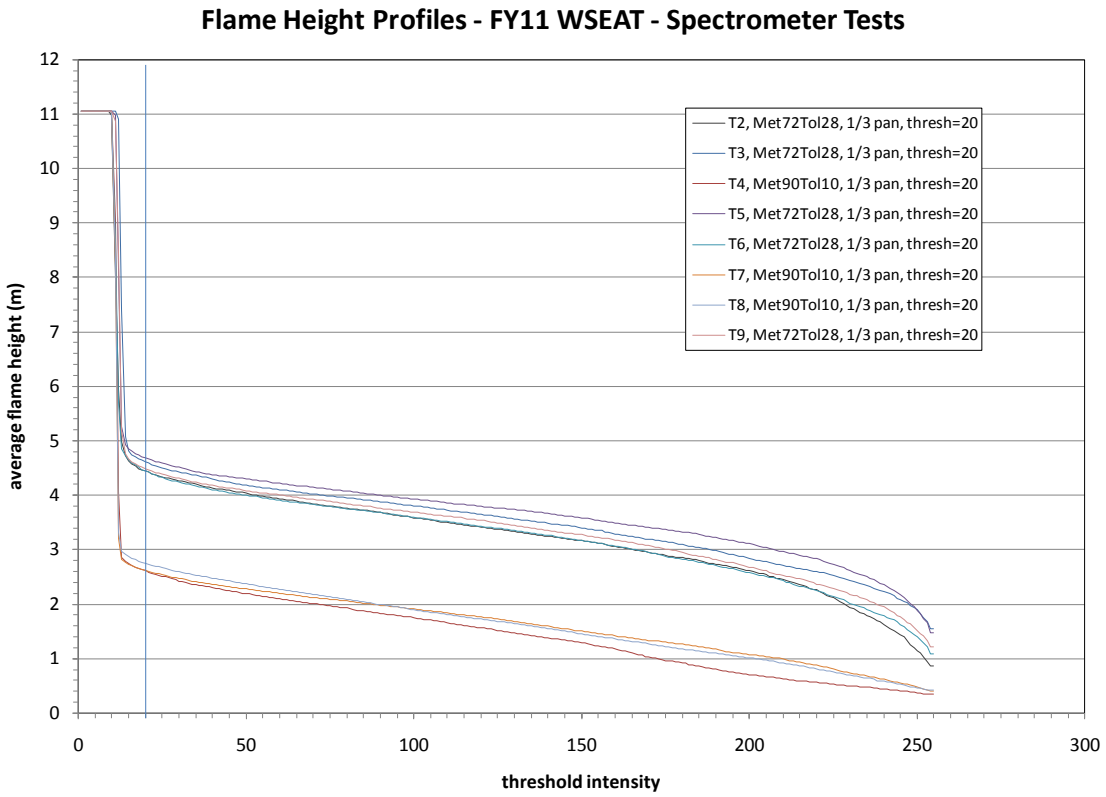

Figure 6 Average flame height as a function of threshold intensity – all datasets.

With the determination of the average threshold intensity, the medium flame height statistics can be determined. Figure 7 shows the flame height for each frame in T9 using a red intensity threshold of 20 (the threshold used in all tests). The horizontal solid and dashed lines show the average and standard deviation of the flame height. The median flame height (where the height is above and below 50% of the time) was also determined.

Table 4 lists the median flame height and the average and standard deviation of the flame height at the start of the spectrometer scan interval for all tests.

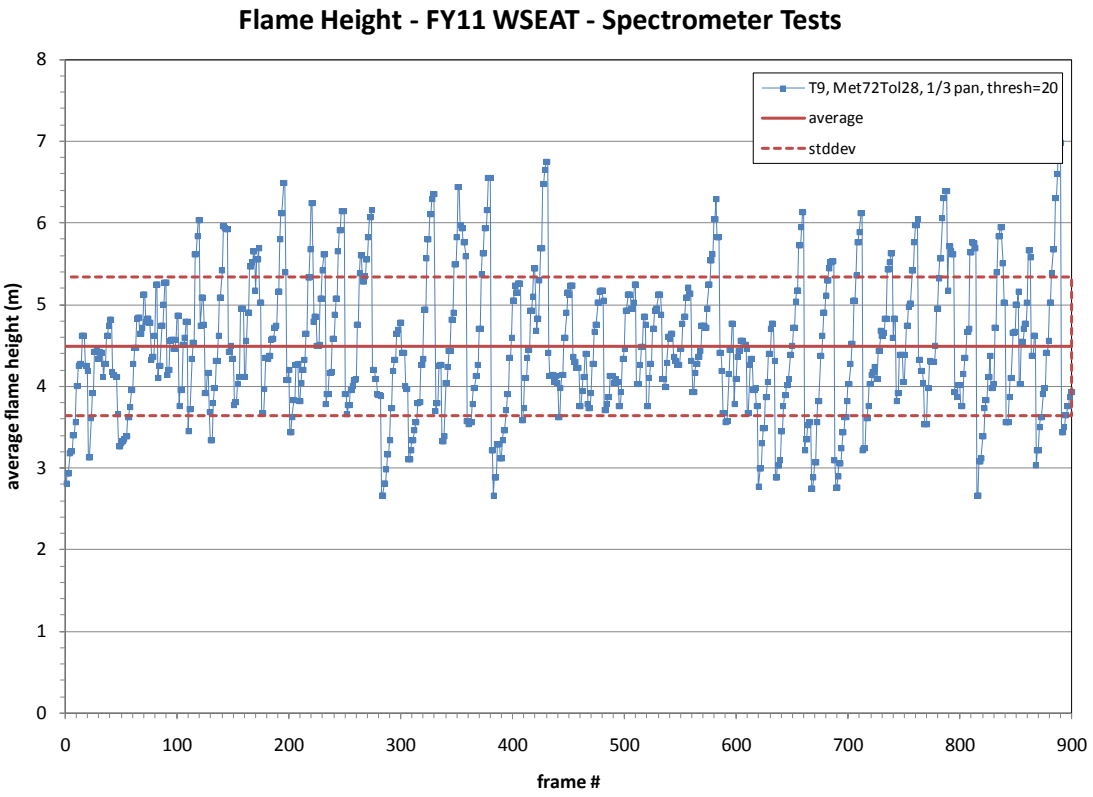

Figure 7 Individual frame flame height (T9).

Table 4 Flame Height Summary

Name	Fuel Mixture	Median Flame Height (m)	Average Flame Height (m)	Standard Deviation (m)
T2	Methanol72% / Toluene28%	4.37	4.45	0.83
T3	Methanol72% / Toluene28%	4.51	4.62	0.87
T4	Methanol90% / Toluene10%	2.44	2.61	0.67
T5	Methanol72% / Toluene28%	4.62	4.69	0.79
T6	Methanol72% / Toluene28%	4.39	4.45	0.82
T7	Methanol90% / Toluene10%	2.52	2.62	0.60
T8	Methanol90% / Toluene10%	2.63	2.74	0.59
T9	Methanol72% / Toluene28%	4.37	4.49	0.85

The flame width as a function of height was measured in two tests (T2 for the azeotrope fuel and T7 for the Methanol90%/Toluene10% fuel mixture). The flame width data are presented in Section 6 and compared against the intensity scan measurements.

3.3.2 *Fuel Regression Rates*

The liquid level control system is shown in Figure 8. Fuel was supplied to the pan from a standard 270 gallon tote located outside the FRH test chamber. The tote sat on a scale (Doran Model XLS/ISAC 9000) with a 4 ft by 4 ft base to fit inside a spill pallet, manufactured by Doran Scales, Batavia IL. A positive displacement Alsco drum pump (model 2998 with 53 gpm (200 lpm) rated flow) drew fuel continuously out of the supply tank at a rate that was greater than the burning rate. The fuel that was not needed to maintain a constant amount of fuel in the pan was returned to the supply tank. The amount of fuel in the pan was inferred from differential pressure measurements made by a Rosemount Model 3051 differential pressure gauge and monitored by a Red Lion programmable controller. When the differential pressure measurement fell below the lower set point the controller opened a control valve (ASCO EF8210B054 1 inch solenoid valve) to feed the pan through a ¾ in. (inner diameter) fuel rated hose. When the differential pressure reading reached the upper set point the controller closed the control valve and the entire flow of fuel drawn out by the pump was simply returned to the supply tank. A second, identical Rosemount 3051 differential pressure gauge was used for data acquisition purposes because the differential pressure data obtained from the output of the Red Lion controller has reduced resolution.

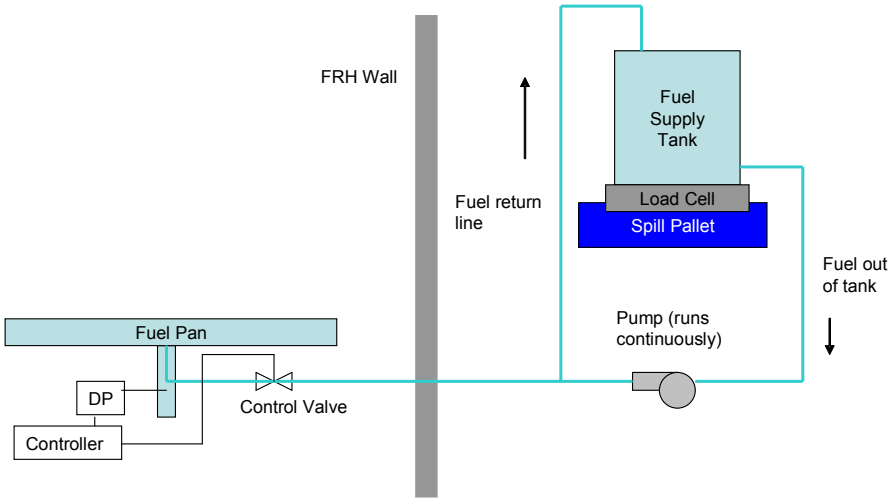

Figure 8 Schematic of the liquid level control system.

To minimize the disturbances to the differential pressure readings caused by the inflow of fuel into the pan, the fuel was not discharged into the pan in close proximity to the DP gauge sensing ports (mounted on the neck of the drain pipe beneath the fuel pan). The fuel is fed up through the drain pipe neck and discharged into the fuel pan using ~20 ft of perforated tubing to distribute the fuel inflow around the pan (not illustrated).

A scale measured the rate of fuel loss from the supply tank over the course of a test. The tote scale has a range of 0 to 2000 lbs (0 to 909 kg) and a resolution of 0.5 lb (0.23 kg). The mass loss rate from the pool was found directly from the change in mass of the

supply tank with time. The fuel regression rate was then determined based on the mass loss rate, the area of the fuel pan, and the density of the fuel.

3.3.3 *Liquid Level Control and Fuel Temperatures*

The test series was performed with a liquid level control system designed to maintain a constant level of liquid fuel in the pan (with ±1 mm of the desired height). Changes in the fuel level have been shown by Orloff and de Ris [1982] to influence the shape and burning characteristics of a fire, which they attributed to tripped turbulence at the lip of the pan.

The liquid level and the temperature distribution across the depth of the pan in the fuel pan were monitored using a thermocouple rake. Twenty-seven (27) thermocouples (type-K, mineral-insulated, metal-sheathed (Inconel), 0.040 inch diameter) were mounted on a steel rake with positions in the fuel pan as indicated in Figure 9. Note the majority of the spacing is 1 mm, to allow fine control of the fuel level.

For each test, the fuel DP controller was initially set based on the estimated fuel regression rate (~146 g/s, 46.5 g/m^{2}s for the azeotrope fuel in the 2 m pan). After fuel ignition, slight adjustments to the controller set point were performed to set the fuel level to the desired level in the pan. The liquid level was easily determined by plotting the temperatures from the thermocouple rake; with a temperature gradient for the fuel in the subcooled regime, at the boiling point (the fuel surface), and superheated fuel in the vapor dome above the liquid surface.

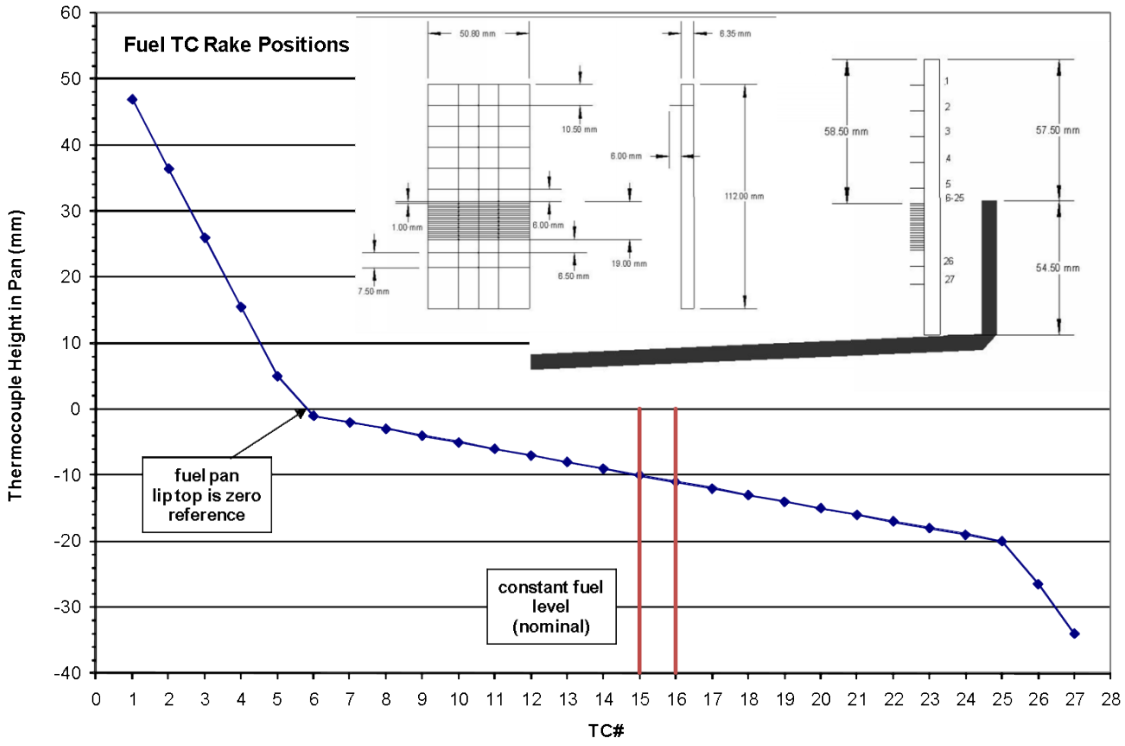

Figure 9 Thermocouple positions in fuel pan.

As an example of the process, Figure 10 presents the fuel pool temperature data during T9. Fuel at ~16 ºC is being added to the pan. At steady-state, the liquid surface is between TC15 and TC16. Thermocouples at and just below the surface measure liquid fuel boiling temperature, ~60ºC. Thermocouples above the liquid surface show an increase in temperature with height into the vapor dome. Figure 10 also presents the drum scale measurement showing the discharge of fuel into the pan and also the fiducial (fidu) signals that occur when the spectrometer collects a measurement (the 1st scan started at ~10 min and the 2nd scan started at ~24 minutes).

Table 5 lists the liquid level in the fuel pan (as denoted by thermocouple positions) during the spectrometer scan interval for all tests.

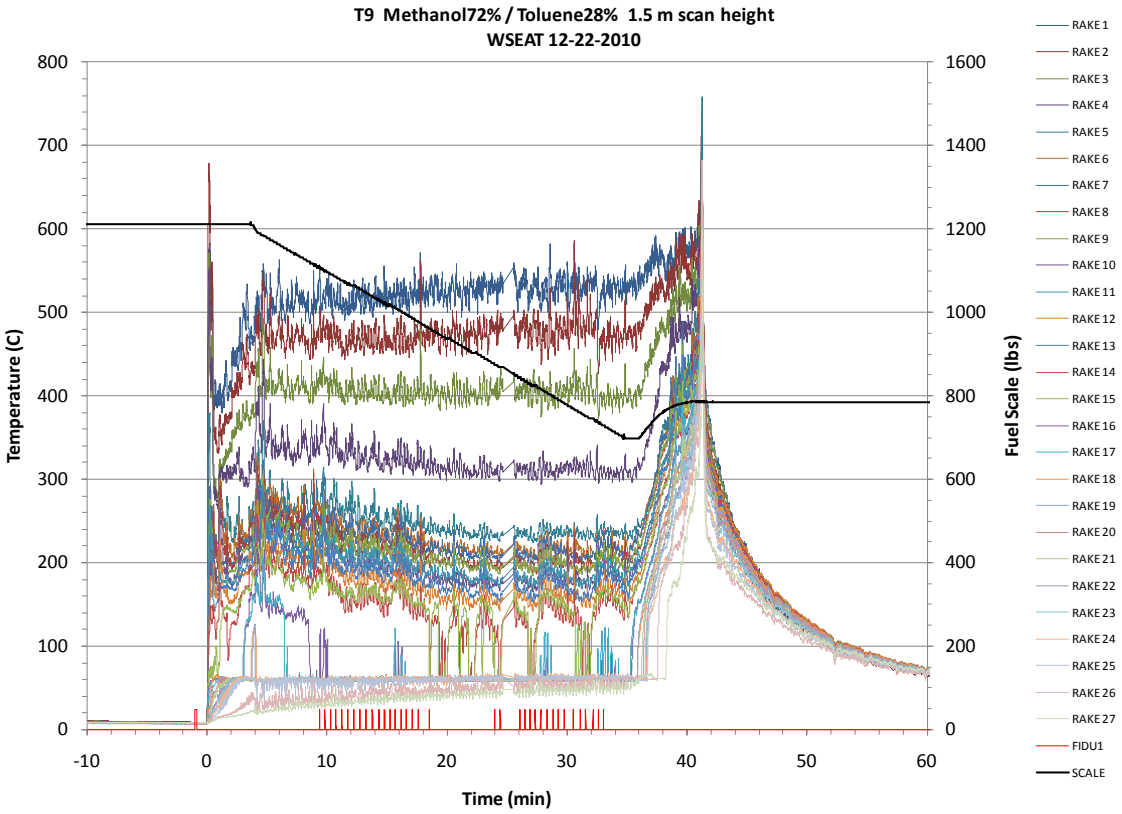

Figure 10 Fuel Thermocouple Rake Response.

Figure 11 shows the differential pressure measurement (inches water column x 1000) used to infer the constant level of fuel in the pan. The fire was determined to be at a steady-state condition at ~10 minutes into the test based on wall-mounted radiometers. Note that there is essentially no change in DP during the steady-state portion of the test. The fuel DP controller was turned off at t = 34 minutes to allow the fuel in the pan to burn out (note some fuel was recovered back into the fuel tote as indicated by the increasing scale measurement), and the remaining liquid in the fuel pan was dumped to the drain tank at t = 41 m.

A scale measured the rate of fuel loss from the supply tank over the course of a test. The scale had a range of 0 to 1000 lbs (0 to 455 kg) and a resolution of 0.25 lb (0.11 kg). The fuel drum weight measurement (lbs fuel) is also shown in Figure 11. The fuel regression rate was determined by dividing the burn rate (the curve fit at steady state is shown in Figure 11, ~16.06 lb/min) by the fuel pan area (3.14 m^2) and the fuel density (814 kg/m^3, estimated from mixture rules). The mass loss rate from the pool is determined by multiplying the fuel regression rate by the fuel density.

In T9, the burn rate was 121.0 g/s (16.0 lbs/min), yielding a mass loss rate of 0.039 kg/m^2s. If not using a constant level fuel system, the fuel regression rate would have been 2.84 mm/min. Equation 1 (with R = 0.0831 bar m^3/kg mol K, T_{boil} = 331K, P = 0.834 bar) was used to determine a vapor velocity (useful for code simulations) of 0.032 m/s.

$$V_{vap} = \frac{\dot{m}''RT_{boil}}{P} \qquad (1)$$

Table 5 lists the burn rate measurements during the spectrometer scan interval for all tests.

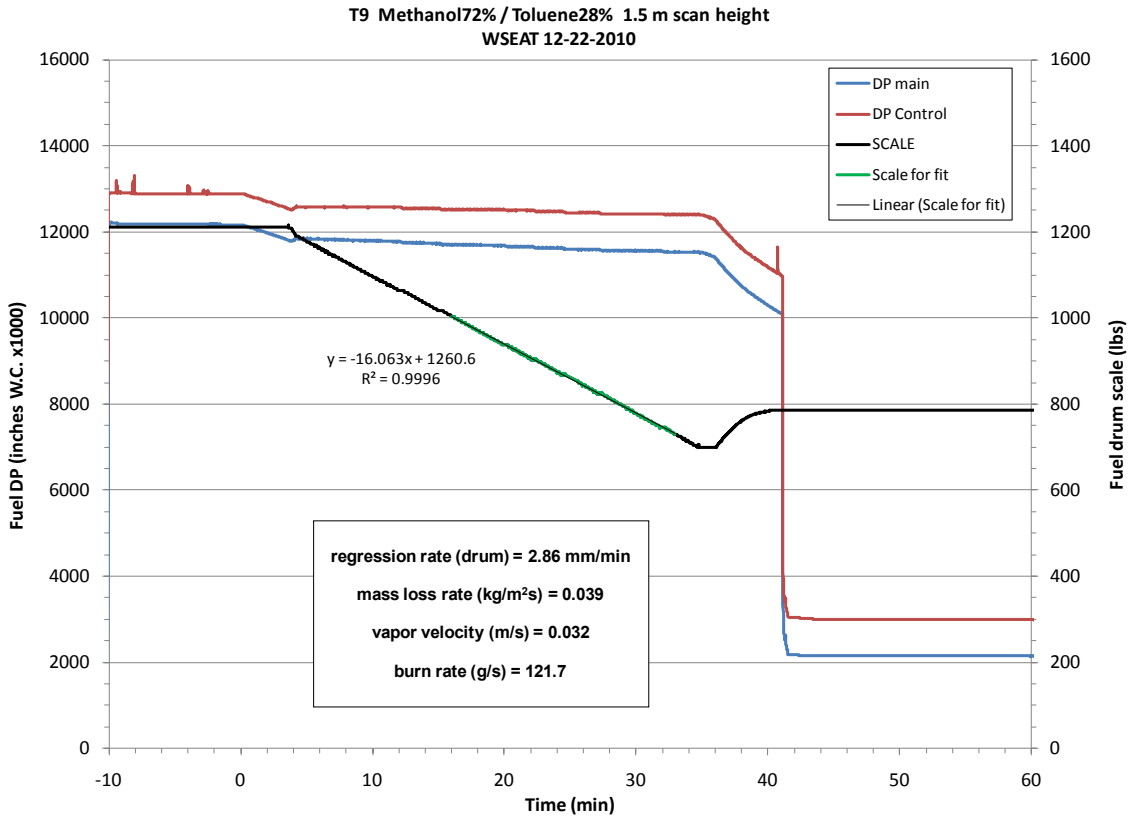

Figure 11 Fuel Burn Rate Parameters.

3.3.4 *Flame Plume Surface Emissive Power*

One narrow-angle radiometer (Medtherm model NVRW-15-5-360-2183, 1º view angle, ZnSe window, designed for 100 kW/m^2 but calibrated to 193 kW/m^2) was used to measure the surface emissive power radiation from the flame plume. The spot diameter for the narrow-angle gauge (at ~9 m) is about 0.16 m.

A total heat gauge (Medtherm model 64-2-18 with a view angle of 180º, range 15 kW/m^2) was mounted adjacent to the other gauge, near the FLAME wall at a distance of ~9 m from the center of the fire to measure the hemispherical heat flux to the wall. The two gauges were mounted side by side at a height of 0.5 m above the pool surface. The line of sight for each gauge passed through the centerline of the fire at the height of the gauge. All of the heat flux gauges were water-cooled. Figure 12 shows that the average surface emissive power was ~90 kW/m^2 and the incident heat flux to the wall was ~1.4 kW/m^2 in T9.

Table 5 lists the average SEP and wall heat flux during the spectrometer scan interval for all tests.

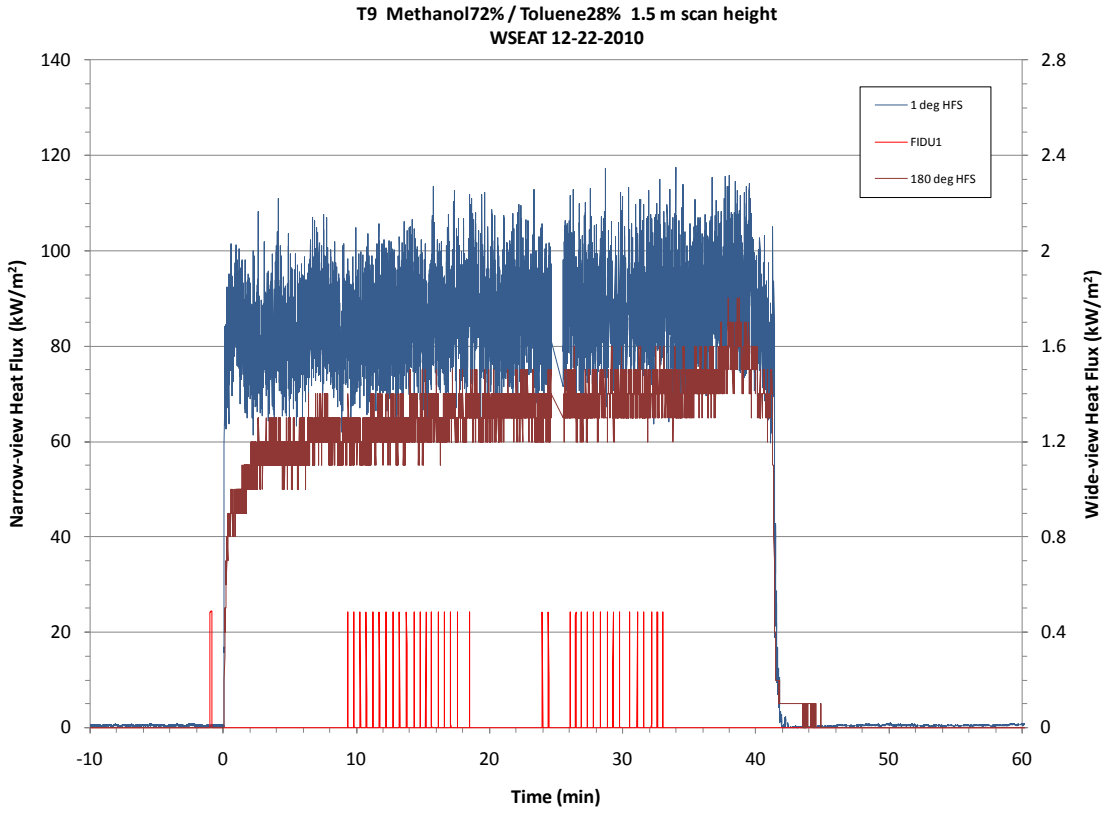

Figure 12 Narrow- and wide-view incident heat flux measurements.

3.3.5 Combustion Air Flow Rate and Temperature

The coflow air supplied to the FRH test cell was controlled to maintain a constant flow rate at the desired value. A forced-draft fan forces air into the chamber at the specified flow rate. An induced-draft fan in the exhaust duct helps to draw air and combustion products out of the chamber and maintains the pressure in the FRH cell at ambient levels. Both fans are computer controlled and the flow rate, fan speed, and current for each fan are logged. The air temperature (listed in Table 5) was measured by a thermocouple in the basement of the FRH facility. The air flow was set to 70,000 scfm for all tests.

3.3.6 Wall Temperatures

The temperatures of the steel walls of the FRH chamber were measured by thermocouples mounted at heights of 1 ft (30 cm), 10 ft (3.04 m), 20 ft (6.08 m), 30 ft (9.12 m), and 39 ft (12.16 m) above the steel grating. The thermocouples were shielded from the radiation from the fire and the convective flow of the coflow air by a small piece of metal foil to minimize bias errors in the wall temperature measurement. These measurements were duplicated at four equally-spaced angular locations around the facility. The wall temperature measurements are of interest for imposed boundary conditions in validation simulations. Figure 13 shows that the FLAME wall temperatures increased ~5-15°C in T9, typical of all test using the azeotrope fuel. The FLAME wall temperatures increased ~2-5°C in those tests using the Methanol90%/Toluene10% fuel mix.

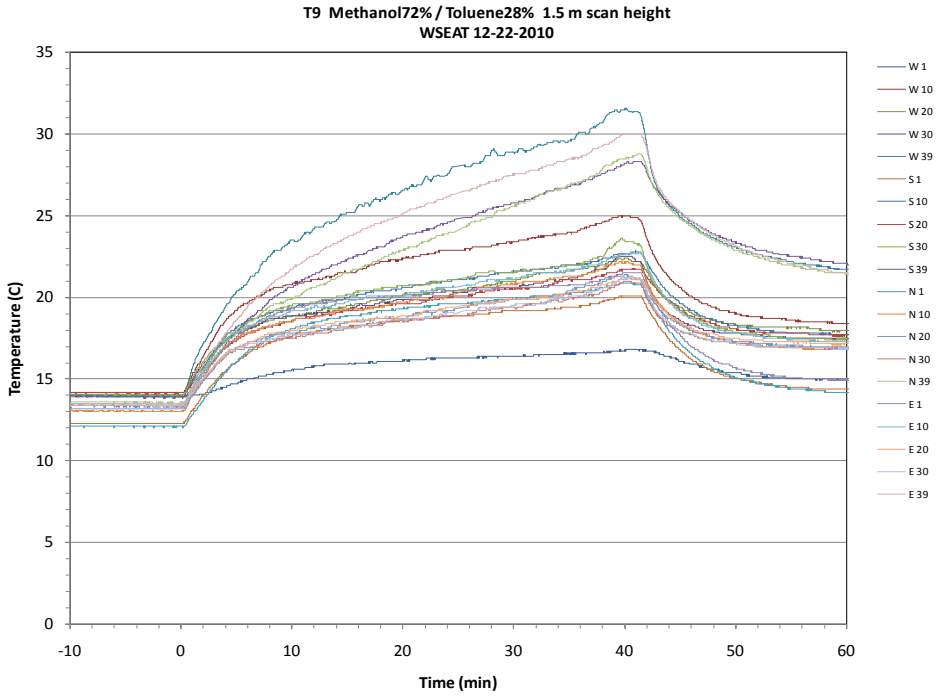

Figure 13 Temperature Response on the FLAME Wall.

Table 5 Summary of the Boundary Conditions, Burn Rates, and Heat Flux

Name	Fuel Mixture	Spectrometer Scan Height Above Pool (m)	SS Interval for Intensity Measurement (min)	Fuel Level between TCs	Inlet Fuel Temp (C)	Inlet Air Temp (C)	Fuel Regression Rate (mm/min)	Fuel Mass Loss Rate (kg/m^2s)	Fuel Vapor Velocity (m/s)	Fuel Burning Rate (g/s)	Fuel Burning Rate (lbs/min)	Surface Emissive Power (kW/m^2)	Wall Heat Flux (kW/m^2)
T2	Methanol72% / Toluene28%	0.5	19 - 33	8-9	62	8	2.88	0.039	0.033	122.8	16.2	88.7	1.4
T3	Methanol72% / Toluene28%	0.5	13 - 45	13-14	9	12	2.86	0.039	0.033	121.9	16.1	83.7	1.4
T4	Methanol90% / Toluene10%	0.5	14 - 42	14-15	6	8	1.63	0.019	0.018	59.5	7.8	41.4	0.3
T5	Methanol72% / Toluene28%	1	9 - 42	13-14	10	15	2.86	0.039	0.032	121.8	16.1	88.3	1.4
T6	Methanol72% / Toluene28%	1	10 - 46	13-14	7	6	2.92	0.040	0.033	124.3	16.4	88.4	1.3
T7	Methanol90% / Toluene10%	1	7 - 33	14-15	7	4	1.63	0.019	0.018	59.3	7.8	43.6	0.3
T8	Methanol90% / Toluene10%	1.5	10 - 35	13-14	8	11	1.65	0.019	0.018	59.9	7.9	43.8	0.4
T9	Methanol72% / Toluene28%	1.5	16 - 33	15-16	8	9	2.86	0.039	0.032	121.7	16.1	86.9	1.3

4. UNCERTAINTY ANALYSIS

An uncertainty analysis for all measurements was performed. The methodology typically followed Coleman and Steele [1999]. Bias errors which can be mathematically modeled, such as the bias error in thermocouple measurements in the fire, were algebraically added to the measurement and the uncertainty in the estimation of the bias was treated as a random error [Romero et al., 2005].

4.1 Fuel Regression Rates

The fuel regression was determined from the rate of change of mass of a fuel supply tank (previously described). The constant-level control system matched the average rate of mass loss from the supply tank to the averaged mass loss rate from the pool, but fuel is supplied to the pan at a rate greater than the regression rate when the control valve is open and is not supplied to the pan when the control valve is closed. The nature of the control system dictates that fuel regression measurements should be averaged over periods much larger than the typical cycle time between commanded signals to open the control valve.

The scale used for measuring the rate of change of fuel mass during the course of a test is resolved to 0.5 lb (0.23 kg) with an uncertainty of ±0.57 kg. Uncertainty in the averaged fuel regression rate decreases as a function of the time over which the results are averaged. For a 2 m pool using a fuel mixture of 72.4%methanol and 27.6%toluene, density 814 kg/m^3, with a fuel regression rate of 2.88 mm/min; the total mass loss from the fuel over a 30 minute span was ~210 kg. Since fuel was not supplied to the pan continuously, the uncertainty in the actual amount of fuel added to the pan was assumed to be half the average mass added per cycle. The measured fuel fill cycle rate was 3.6 cycles per minute, yielding an uncertainty due to the unsteady fill rate of ±0.97 kg. If the uncertainty in the pan area, fuel density, and time between measurements are neglected, the total RSS combined uncertainty in the fuel regression rate measurement was ±0.015 mm/min or 0.54%.

4.2 Temperature of Liquid Fuel

An uncertainty analysis for thermocouple data acquisition systems in use at Sandia's Radiant Heat facility and the Lurance Canyon burn site has been performed by Nakos [2004]. The analyses apply to Type K, chromel-alumel thermocouples in MIMS thermocouple assemblies and other applications. Several DASs were analyzed, one Hewlett-Packard (HP) 3852A system, and several NI systems. The uncertainty analyses were performed on the entire system from the thermocouple to the DAS output file. Uncertainty sources include thermocouple mounting errors, ANSI standard calibration uncertainty for Type K thermocouple wire, potential errors due to temperature gradients inside connectors, extension wire effects, DAS hardware uncertainties including noise, common mode rejection ratio, digital voltmeter accuracy, mV to temperature conversion, analog to digital conversion, and other possible sources. Typical results for "normal" environments (e.g., maximum of 300 to 400 K) showed the total uncertainty to be about

±1% of the reading in absolute temperature. In high temperature or high heat flux ("abnormal") thermal environments, total uncertainties range up to ±2-3% of the reading (maximum of 1300 K). The higher uncertainties in abnormal thermal environments are caused by increased errors due to the effects of imperfect thermocouple attachment to the test item.

The ANSI standard uncertainty for Type K thermocouple wire is 2.2ºC or 0.75% of reading (in ºC), whichever is greater. This uncertainty applies to the temperature of the thermocouple junction itself. Determination of the actual desired temperature (wall temperatures of an object or fluid temperatures) is subject to additional bias errors due to mounting. These bias uncertainties are very hard to accurately quantify, are application dependent, and are often the largest errors in the measurement system. For the present tests the bias error in the liquid fuel measurements was assumed to be small compared to the thermocouple uncertainty. The thermocouple was in good thermal contact with the liquid, which has a thermal conductivity much greater than that of air. Furthermore, radiation errors, etc. are expected to be small within the liquid. The local liquid temperature was expected to vary slowly compared to the thermal response time of the thermocouple. The overall uncertainty of the liquid fuel temperatures was assumed to be ±3ºC, which added some conservatism to the ANSI standard uncertainty.

4.3 Air Flow Rate and Temperature

The air flow rate was measured by a Veltron II pressure and flow transmitter (Air Monitor Corporation, Santa Rosa, CA). The Veltron II calculated the air velocity and flow rate based on a differential pressure measurement. The differential pressure was measured to an accuracy of 0.1% of the natural span of the transmitter (10 inches of water). The uncertainty in the velocity due to the differential pressure uncertainty was approximately ±3% at the chosen flow rate of ~70,000 scfm. When the uncertainties due to non-uniformity in the velocity profile, tolerances on the duct dimensions, etc. are included the total uncertainty was estimated to be approximately ±6% of the total flow rate.

Air temperature measurements were performed by thermocouples similar to those used in the liquid fuel measurements. The air temperature measurements were made inside a duct in a relatively cool environment in which convective heat transfer from the air to the thermocouple was expected to dominate, therefore the uncertainty in the air temperature was assumed to be the same as the uncertainty in the fuel temperature measurements, ±3ºC.

4.4 Wall Temperatures

Wall temperature measurements were made by thermocouples mounted to the steel walls of the FRH chamber. The thermocouples were in good thermal contact with the walls, which have a very high thermal conductivity. The thermocouples were partially shielded from the radiation of the fire and convection from the cool coflowing air. Previous experience has shown that the walls remain relatively cool during tests due to their large

thermal mass. The analysis of Nakos [2004] suggests that the maximum error is ±1% of the reading (in K) for temperatures up to 400K. An uncertainty of ±4ºC was assumed for the wall temperatures in the present tests.

4.5 Radiation Intensity in Fires

The manufacturer's stated uncertainty for the Spectraline ES-200 spectrometer was ±0.5% of full range of the signal (0 to 10 Volts), which corresponds to the random error in the measurement. The accuracy of the intensity or the transmission coefficient measurement is then a function of the accuracy and appropriateness of the calibration. With baseline intensity appropriate for a fire, the maximum and minimum reference voltages are estimated for the present analysis to be 1.5 V and 0.5 V. The uncertainty due to the random error in the recorded voltage is then ±0.03 units at the maximum intensity and ±0.10 units at the minimum intensity. If the uncertainty in the reference voltage is assumed to be ±15%, the overall uncertainties is ±0.18 units.

4.6 Average Flame Height

The flame height is defined herein as the median flame height; a height where the flame is above 50% of the time and below 50% of the time, based on automated video analyses. Uncertainty in the actual height of the visible flame in an individual image is estimated to be approximately 10 cm. Uncertainty in determination of the average flame height based on a minimum of 900 video frames will be assumed to be equal to the uncertainty in determining the height of the flame within the frame.

4.7 Heat Flux from the Plume Surface

The incident radiative heat fluxes to objects outside the fire are measured by radiometers, calibrated after assembly by the manufacturer. The uncertainty in the measurement is the total uncertainty in the radiometer calibration. A typical radiative heat flux calibration uncertainty of ±3% was assumed [Nakos 2005].

5. INTENSITY MEASUREMENT RESULTS

The following plots provide the raw data as reduced from the spectrometer. In all tests except for T2, two scans were performed after the fire reached a steady-state condition. The scans are labeled round 1 (R1) and round 2 (R2). The first data point started with the exit of the spectrometer viewing tube at 0.1 m inside the pan lip. At each point, the spectrometer collected 4096 sets of 256 pixel data in ~10.5 s (in T2 the spectrometer scan was set to collect 1280 sets). The viewing tube was then moved into the fire in 10 cm increments (~10 s to move) and the process repeated. After the last data point (either at 1.9 m into the pool or it was obvious that the tube had passed completely through the fire), the tube was withdrawn to the start position and the second scan commenced.

Figure 14 provide the set-average of the intensity as a function of wavelength for all measurement points of the round 1 scan for T2. Figure 15 provides the integrated intensity data as a function of scan distance into the flame plume using Equation 2. Note the spectrometer provided intensity data at 213 wavelengths, ranging between 1.21 μm to 4.89 μm.

$$Integrated\ Intensity = \sum_{w=1}^{213} \left(\frac{I_w + I_{w+1}}{2} \right) \left(w_{i+1} - w_i \right) \tag{2}$$

Where

w_i = wavelength i

I_w = intensity at wavelength w

Figure 16 provides the integrated data normalized over two wavelengths; the first was over the wavelength range 3.2-3.5 microns and the second over the entire spectrometer wavelength range of 1.21-4.89 microns using Equation 3 and described below. At each scan position, the normalized intensity was determined by first dividing the intensity at each wavelength by the maximum wavelength intensity in the scan. Then two averages were performed, one using the range between 3.2-3.5 microns and the second using the range between 1.21 to 4.89 microns. Similar figures are provided for all of the tests.

$$Normalized\ Intensity = Average_{w = 3.2\ to\ 3.5\ \mu m} \left(\frac{I_i}{Max\ I_{w = 1,213}} \right) \tag{3}$$

The T2 test provided a 3 s scan at each location (note that the software locked up at the 1.3 m location). A repeat test (T3) showed nearly identical results with an 11 s scan (scan time increased to determine if puffing was a concern).

5.1 Test 2 - Met72/Tol28 - 0.5 m above Pool (12/1/2010)

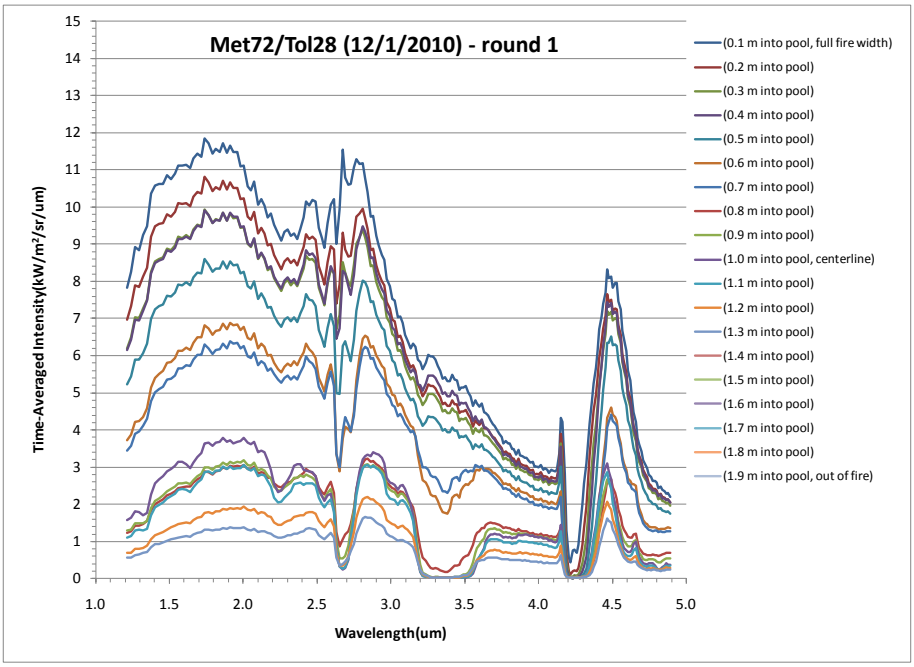

Figure 14 Test 2 Intensity Data – Round 1.

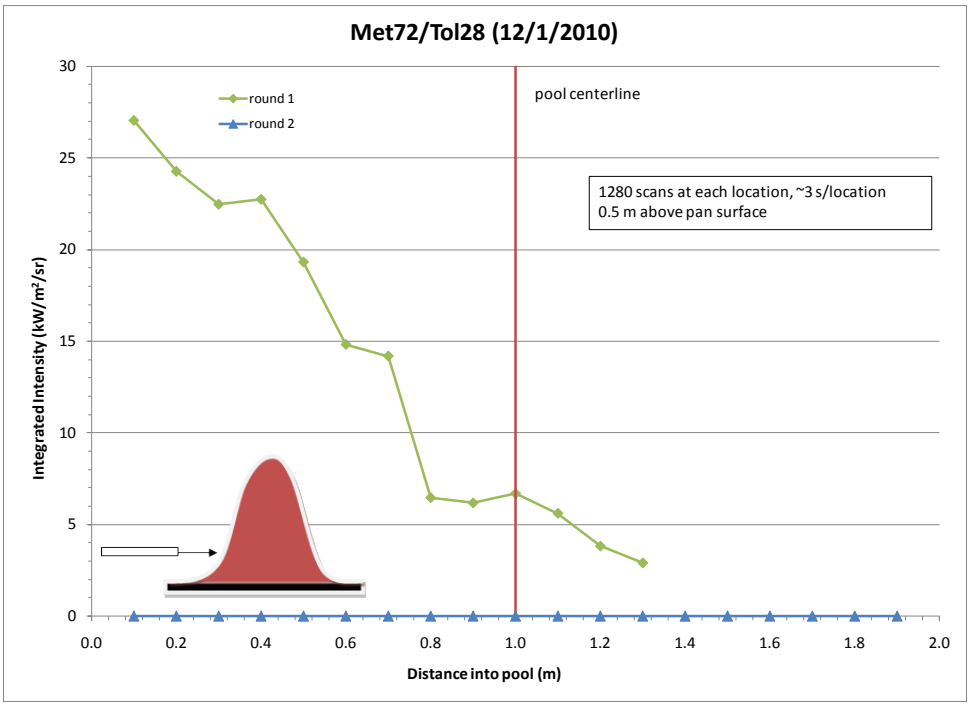

Figure 15 Test 2 Integrated Intensity Data.

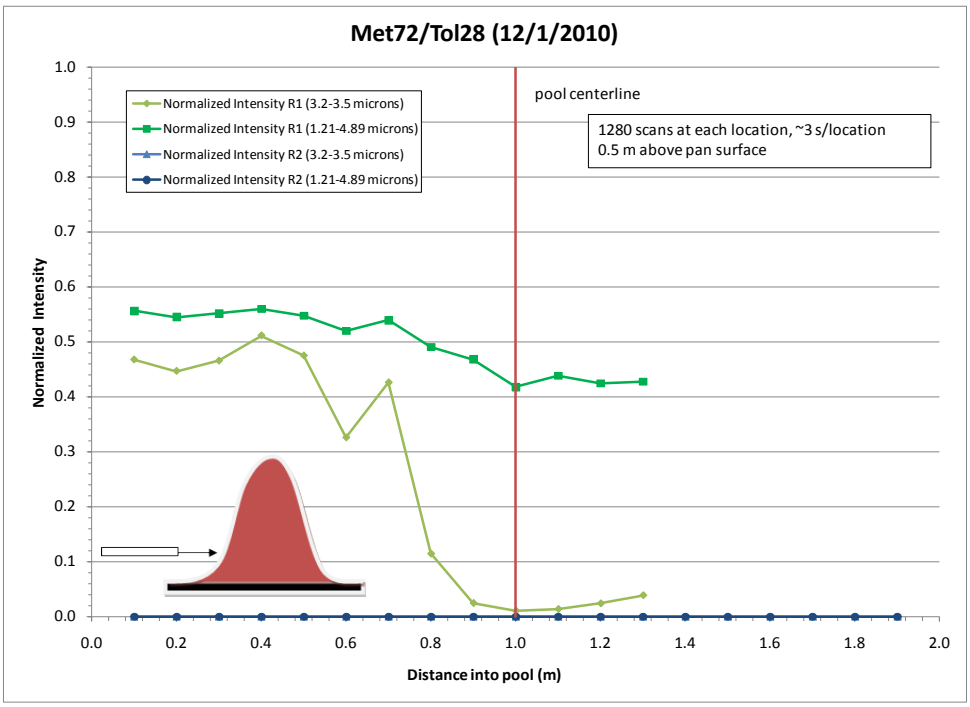

Figure 16 Test 2 Normalized Intensity Data.

5.2 Test 3 - Met72/Tol28 - 0.5 m above Pool (12/7/2010)

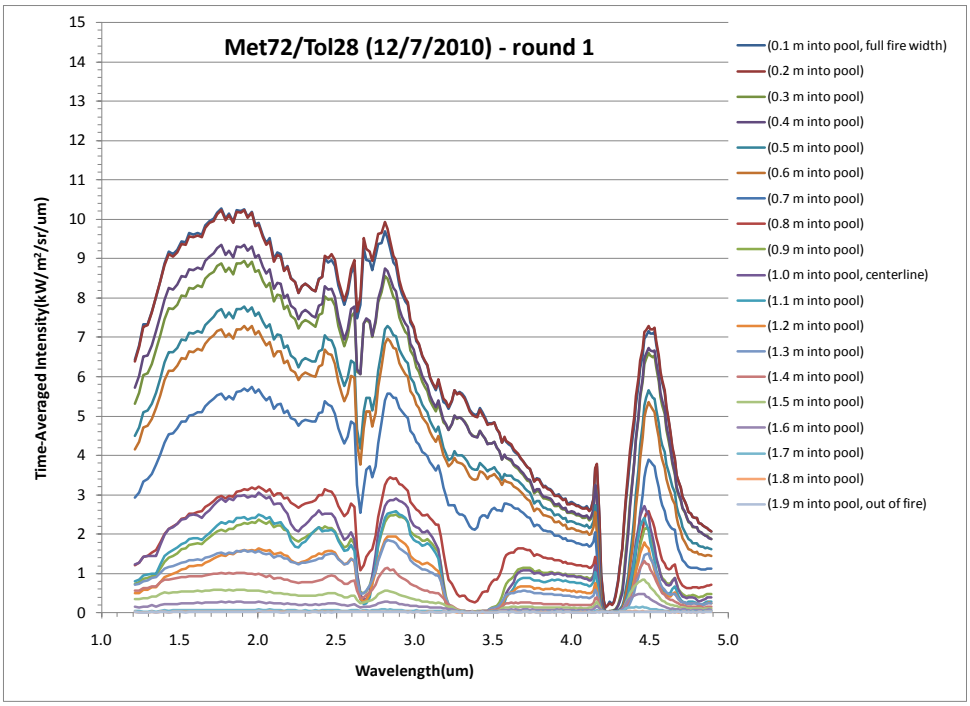

Figure 17 Test 3 Intensity Data – Round 1.

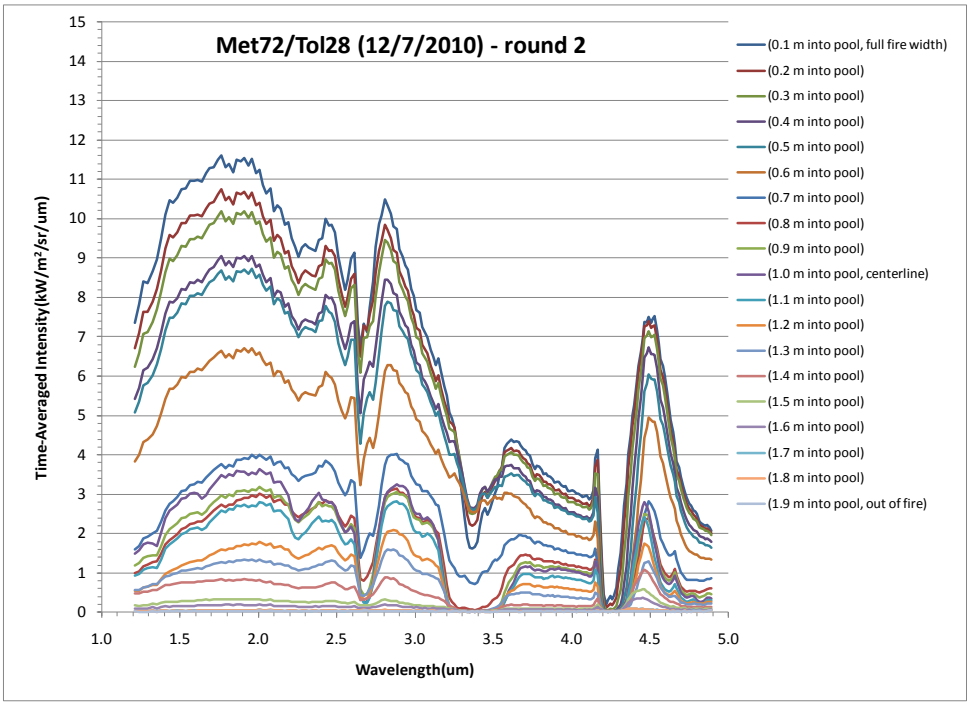

Figure 18 Test 3 Intensity Data – Round 2.

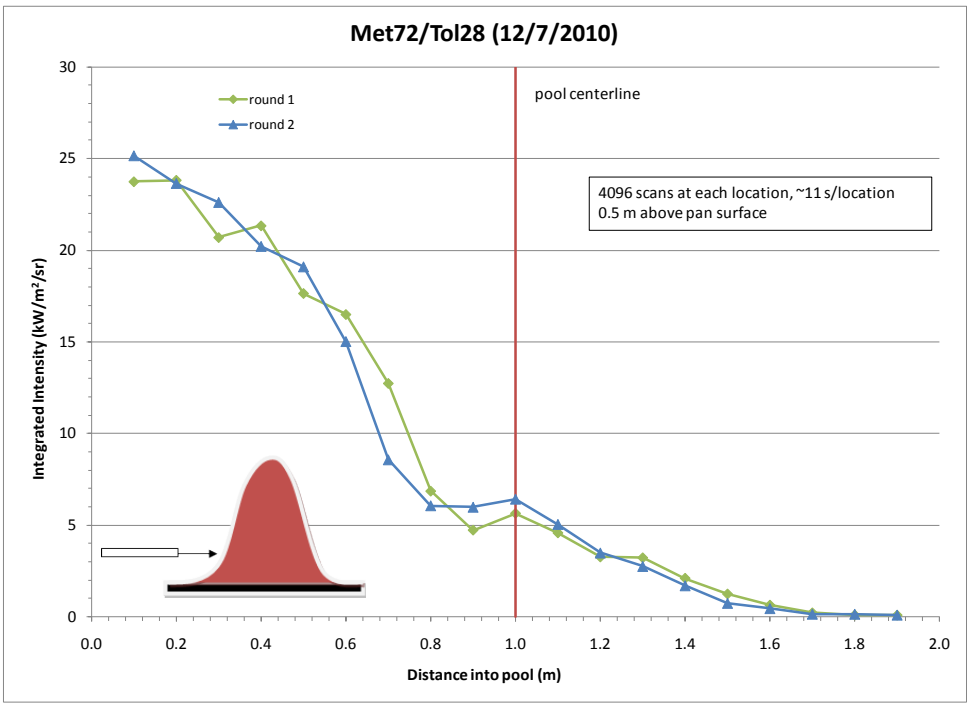

Figure 19 Test 3 Integrated Intensity Data.

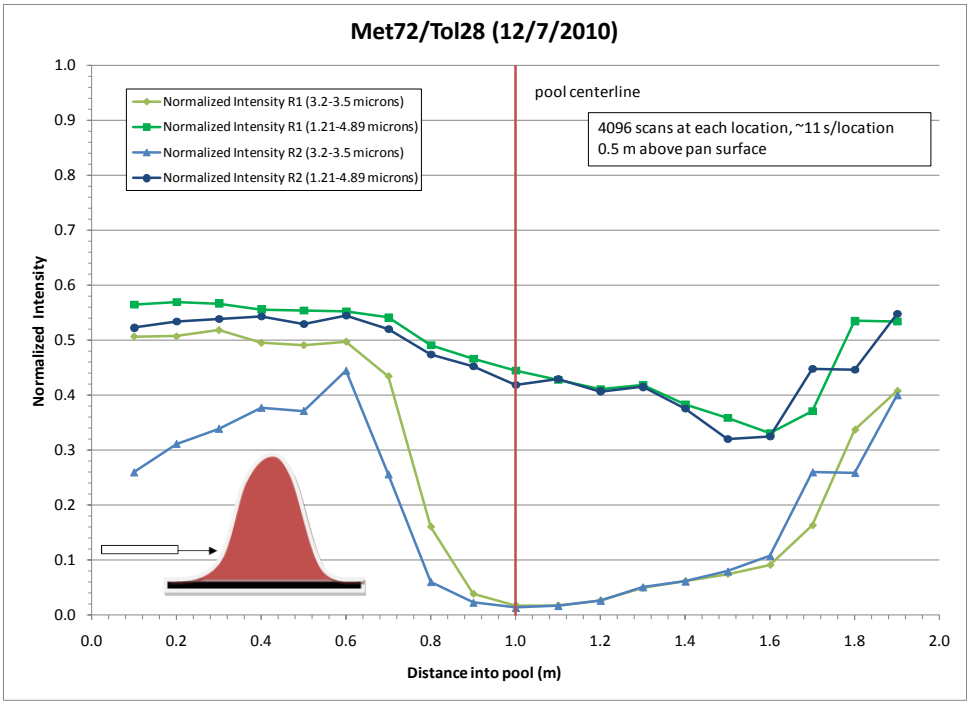

Figure 20 Test 3 Normalized Intensity Data.

5.3 Test 4 - Met90/Tol10 - 0.5 m above Pool (12/9/2010)

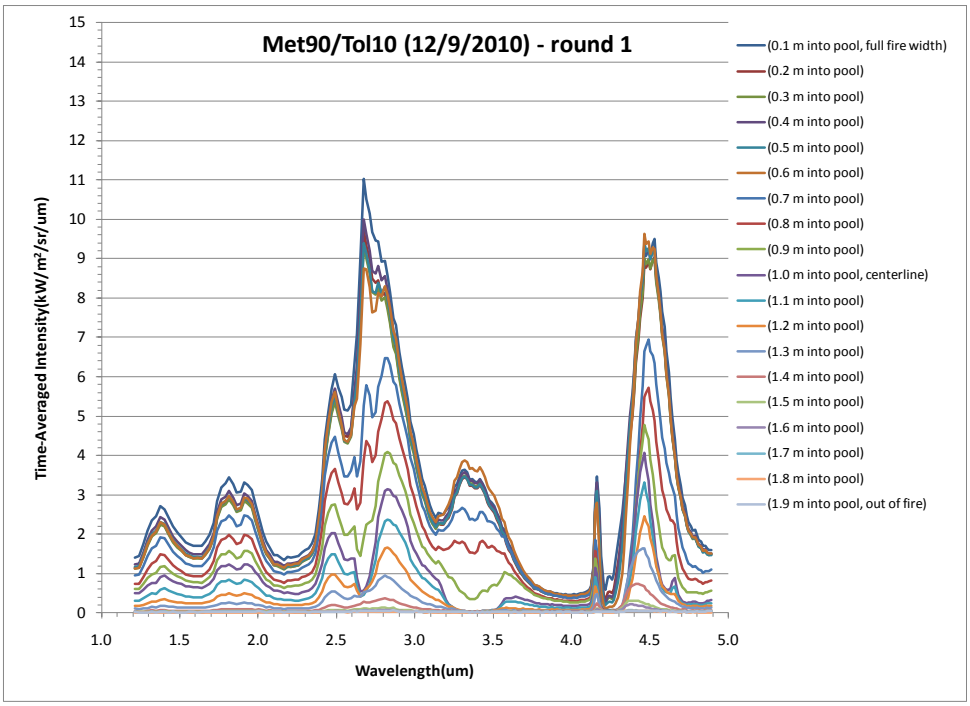

Figure 21 Test 4 Intensity Data – Round 1.

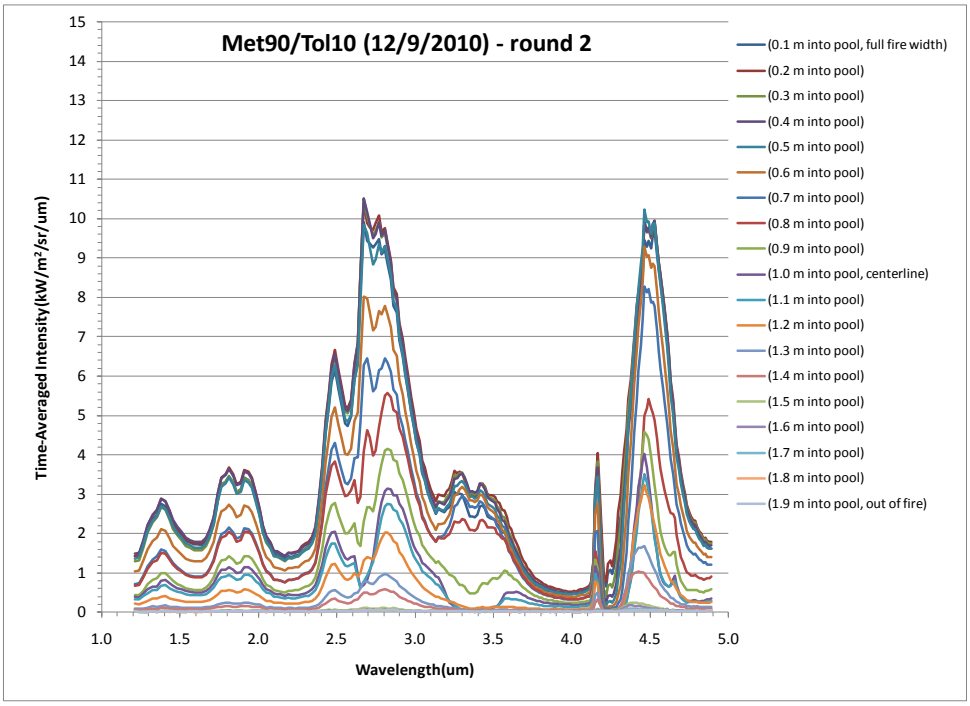

Figure 22 Test 4 Intensity Data – Round 2.

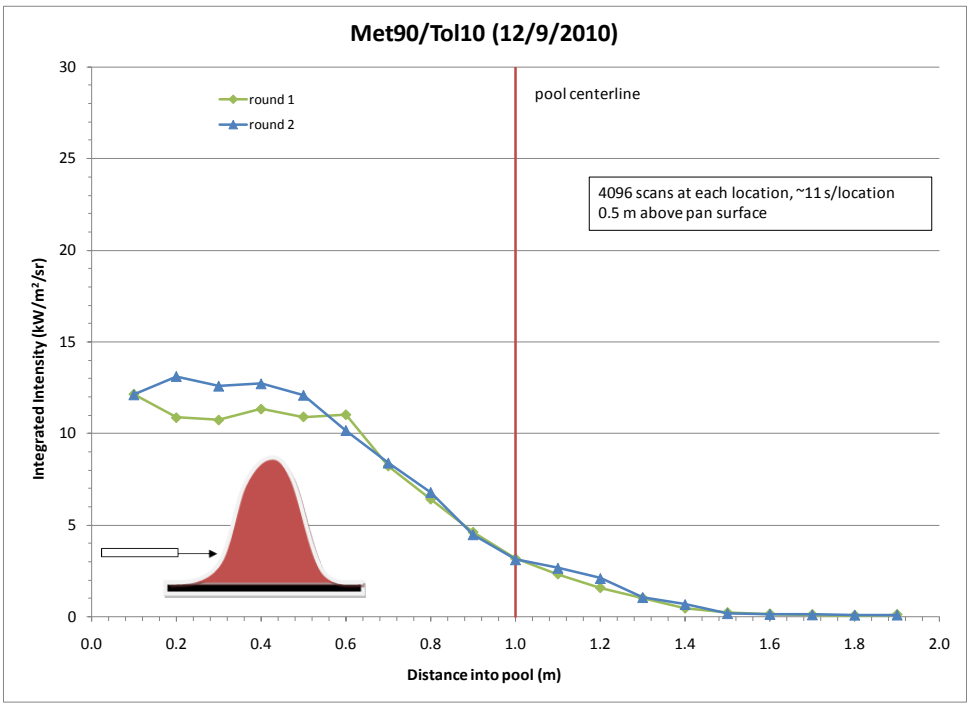

Figure 23 Test 4 Integrated Intensity Data.

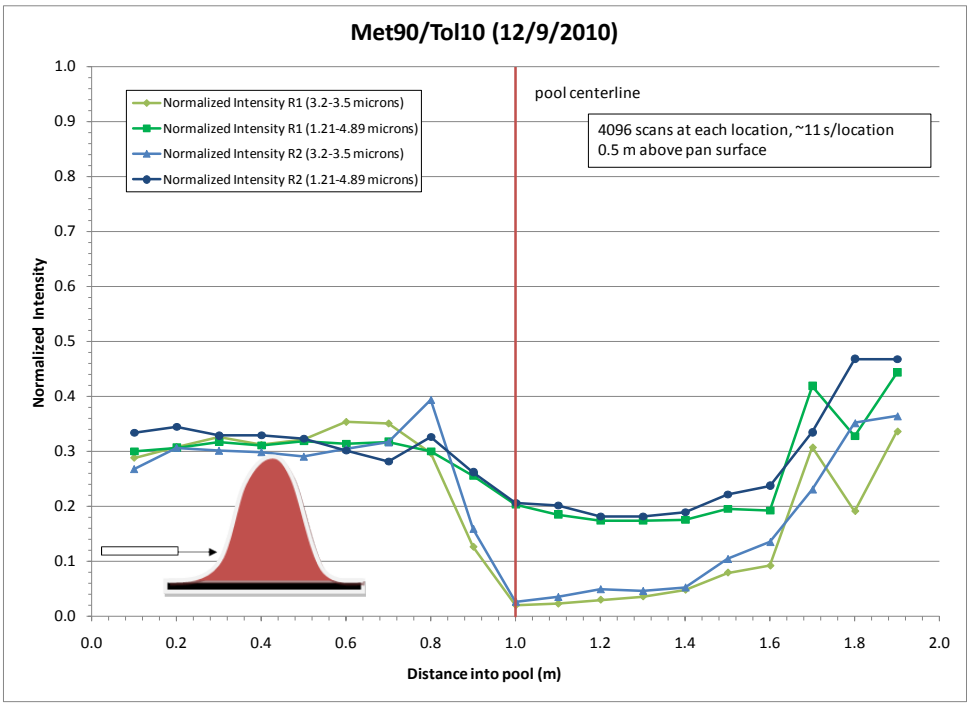

Figure 24 Test 4 Normalized Intensity Data.

5.4 Test 5 - Met72/Tol28 – 1.0 m above Pool (12/15/2010)

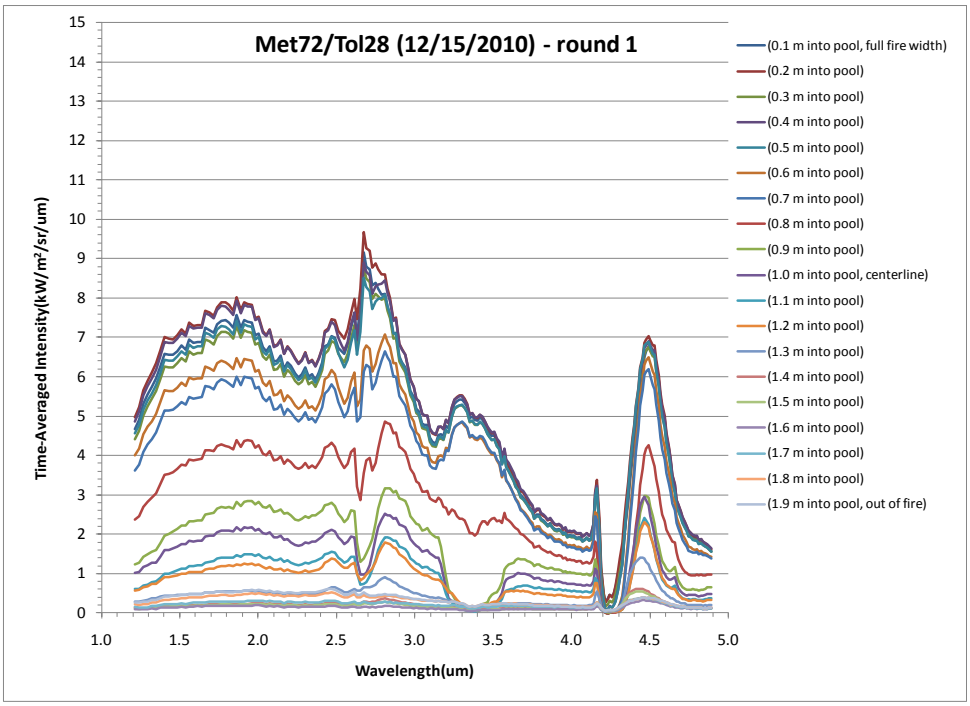

Figure 25 Test 5 Intensity Data – Round 1.

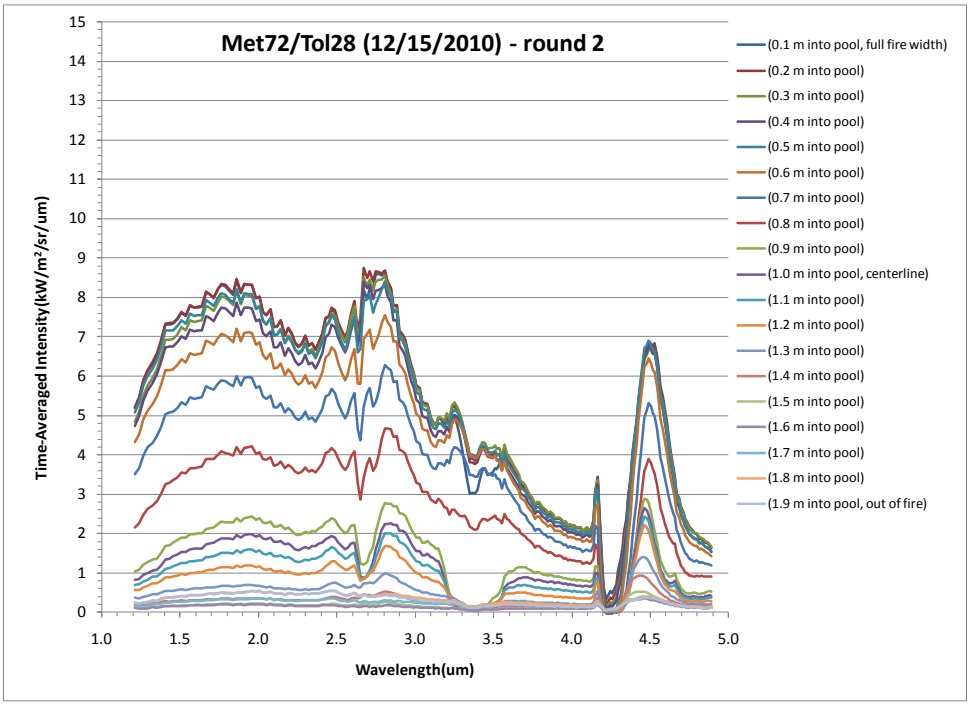

Figure 26 Test 5 Intensity Data – Round 2.

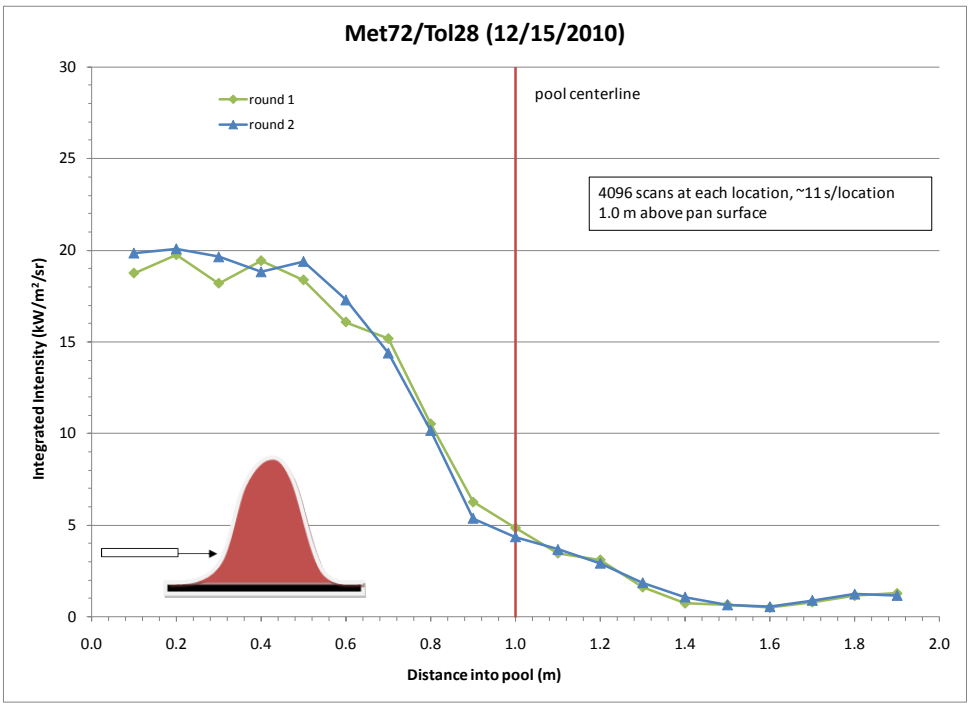

Figure 27 Test 5 Integrated Intensity Data.

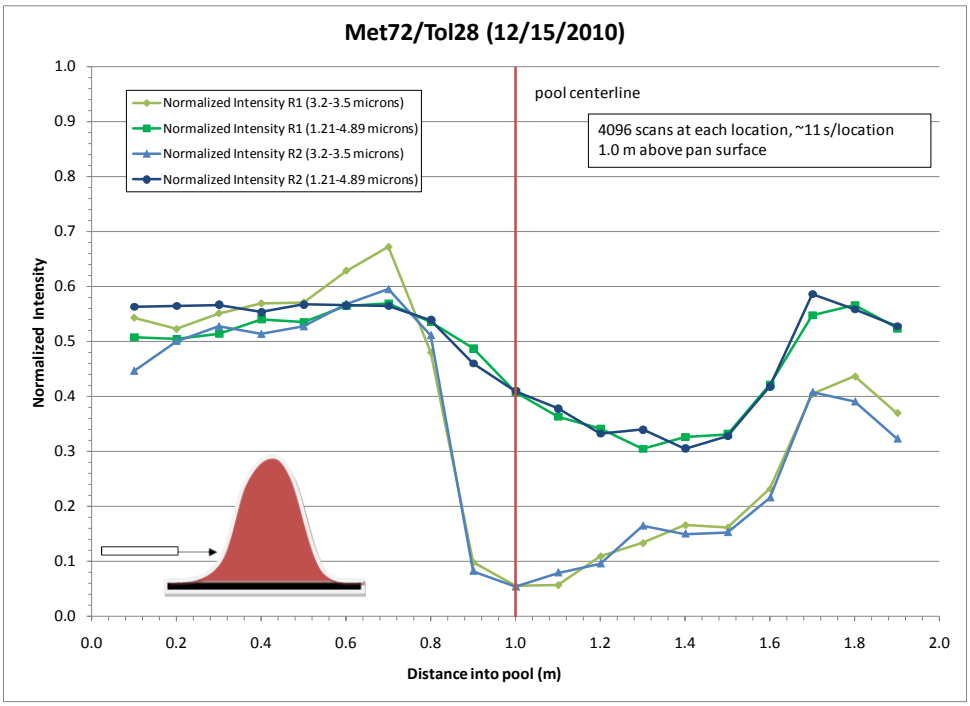

Figure 28 Test 5 Normalized Intensity Data.

5.5 Test 6 - Met72/Tol28 – 1.0 m above Pool (12/16/2010)

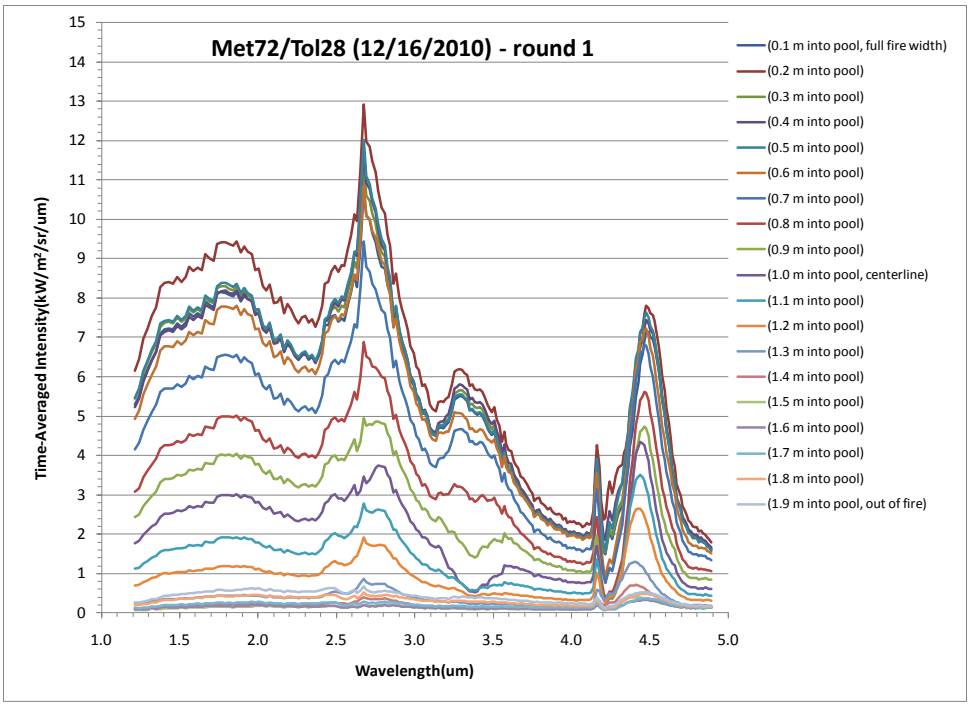

Figure 29 Test 6 Intensity Data – Round 1.

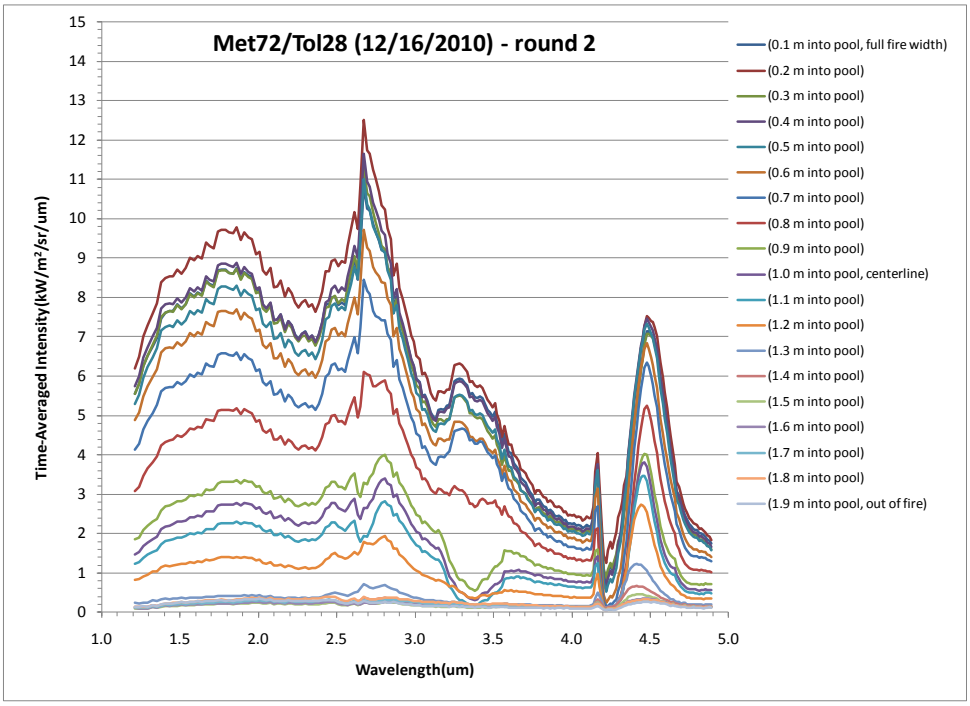

Figure 30 Test 6 Intensity Data – Round 2.

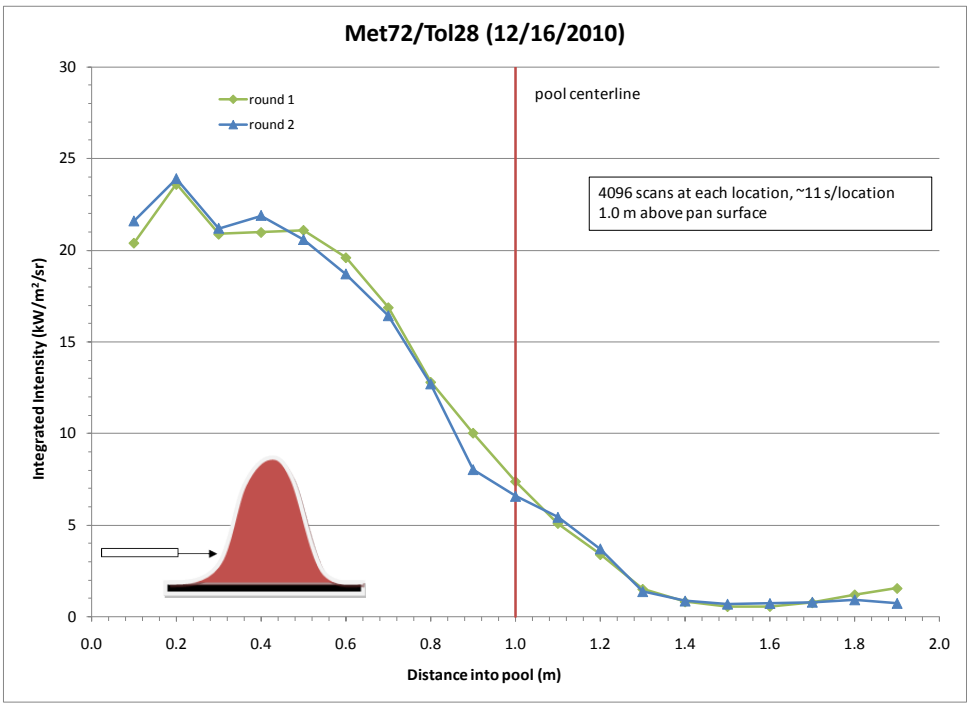

Figure 31 Test 6 Integrated Intensity Data.

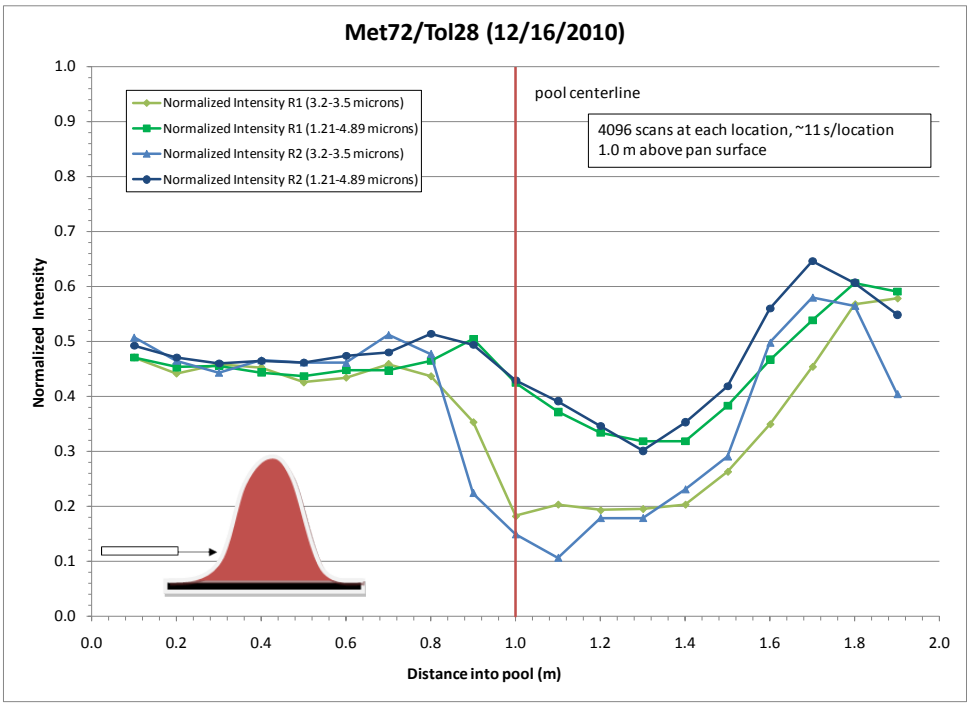

Figure 32 Test 6 Normalized Intensity Data.

5.6 Test 7 – Met90/Tol10 – 1.0 m above Pool (12/16/2010)

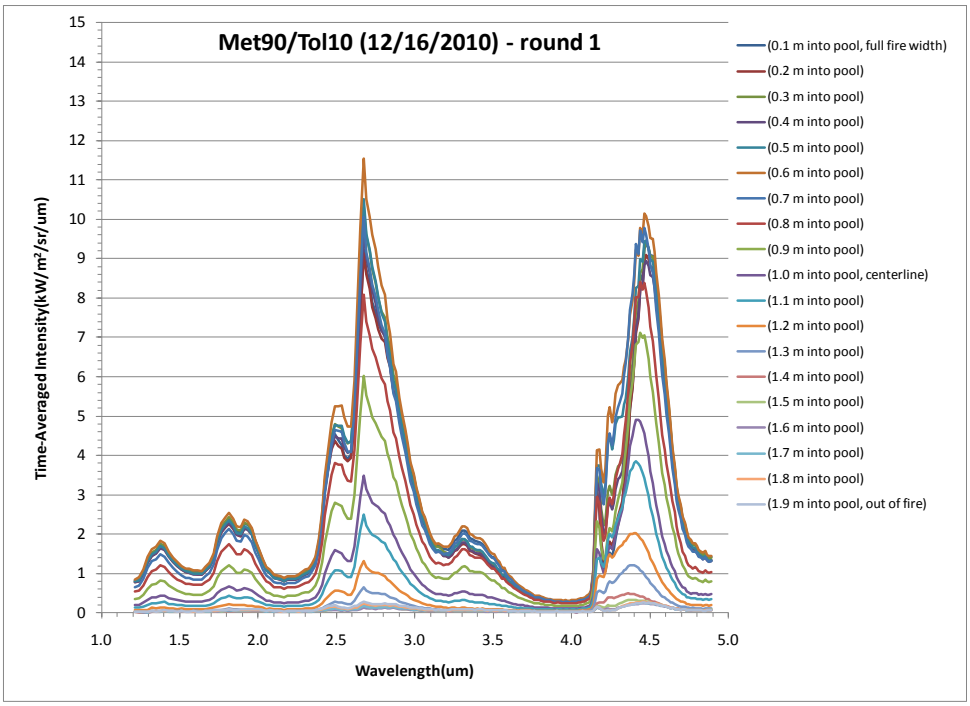

Figure 33 Test 7 Intensity Data – Round 1.

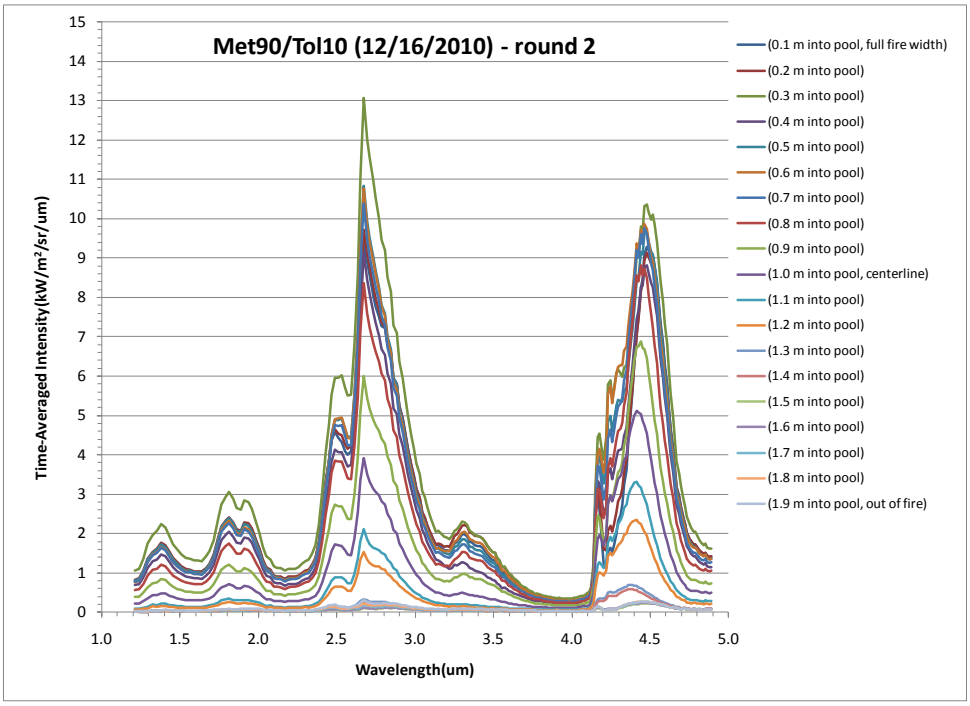

Figure 34 Test 7 Intensity Data – Round 2.

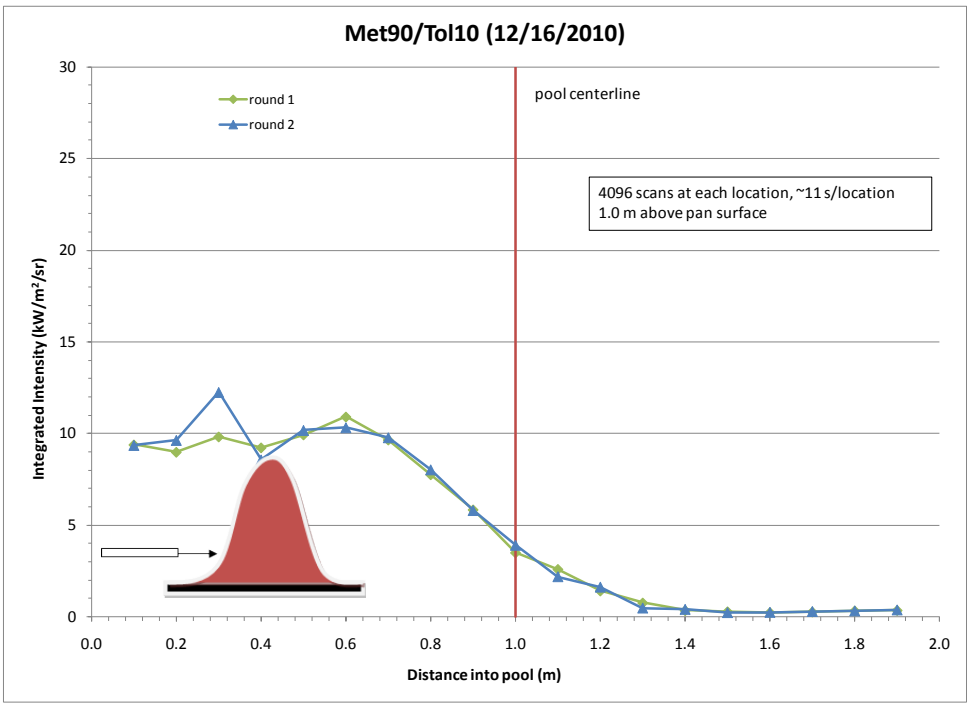

Figure 35 Test 7 Integrated Intensity Data.

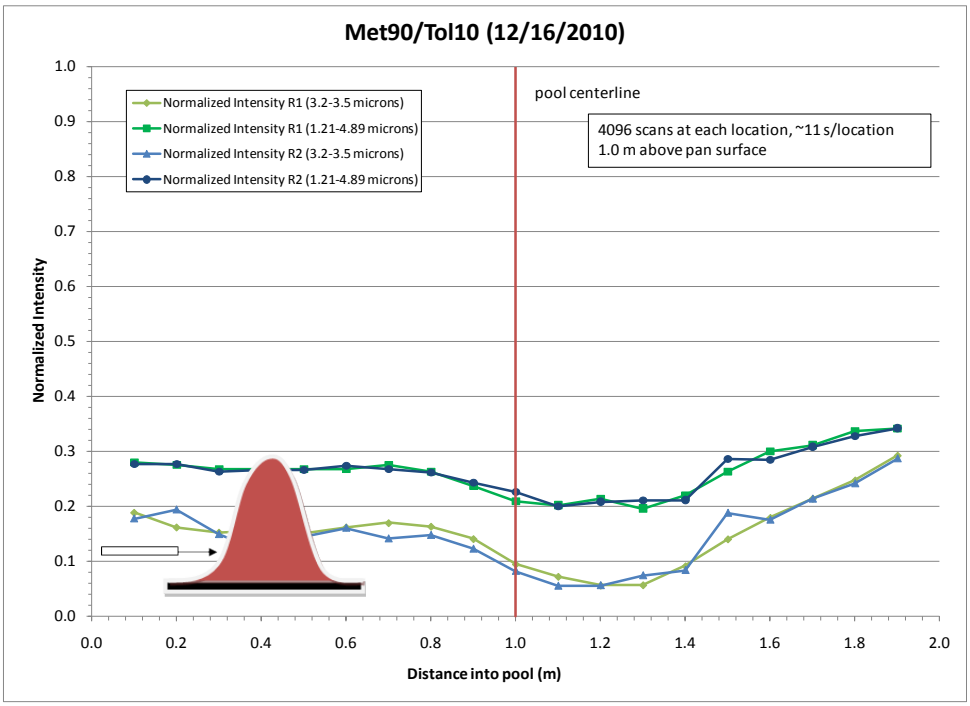

Figure 36 Test 7 Normalized Intensity Data.

5.7 Test 8 – Met90/Tol10 - 1.5 m above Pool (12/21/2010)

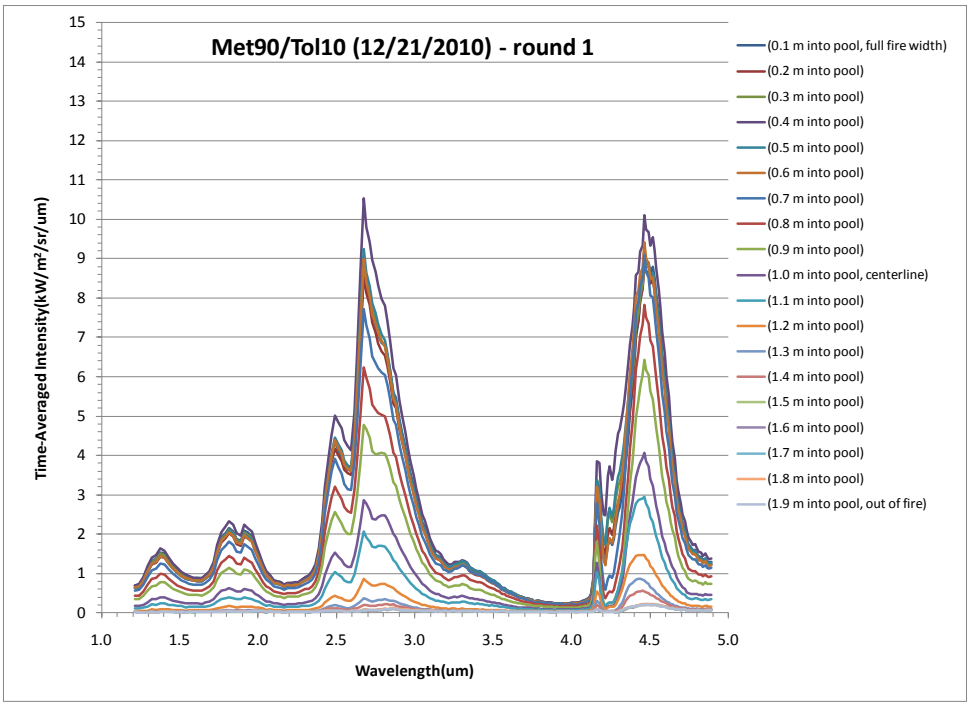

Figure 37 Test 8 Intensity Data – Round 1.

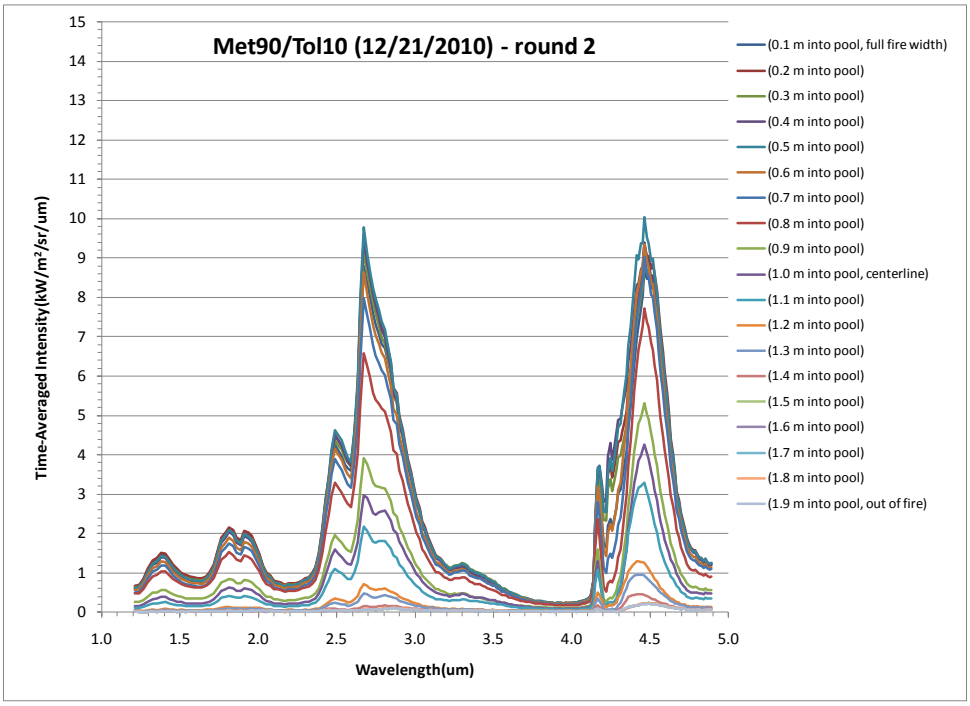

Figure 38 Test 8 Intensity Data – Round 2.

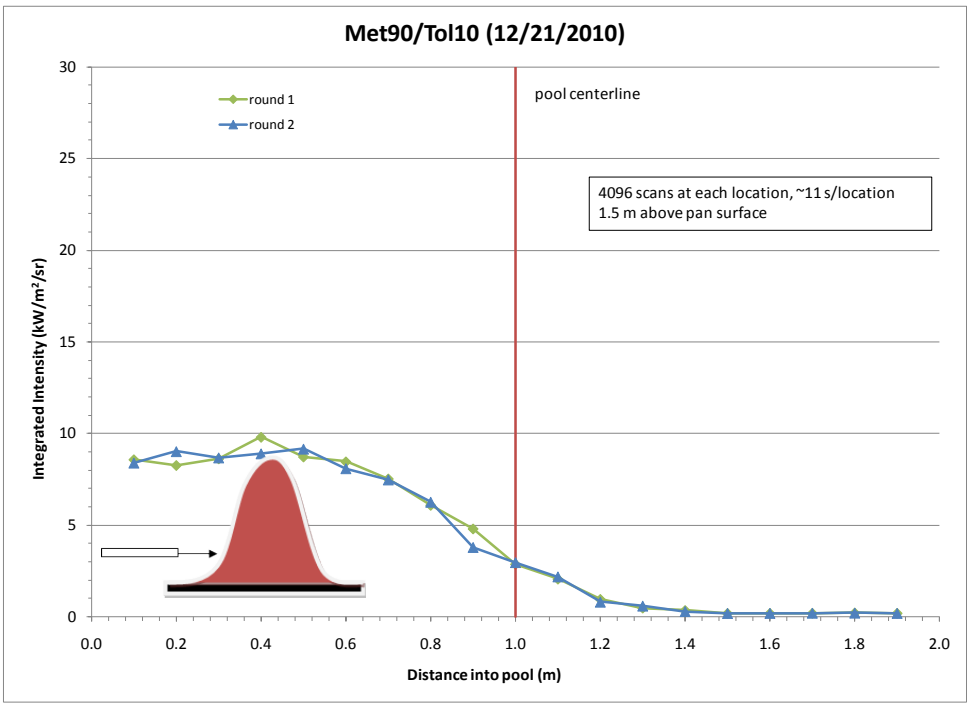

Figure 39 Test 8 Integrated Intensity Data.

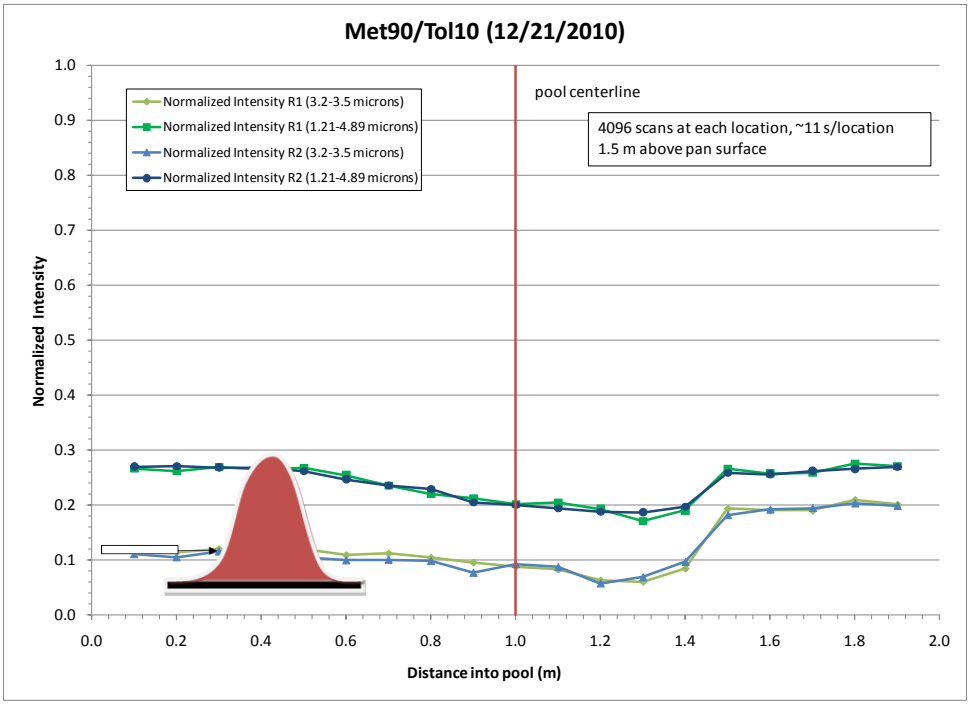

Figure 40 Test 8 Normalized Intensity Data.

5.8 Test 9 - Met72/Tol28 - 1.5 m above Pool (12/22/2010)

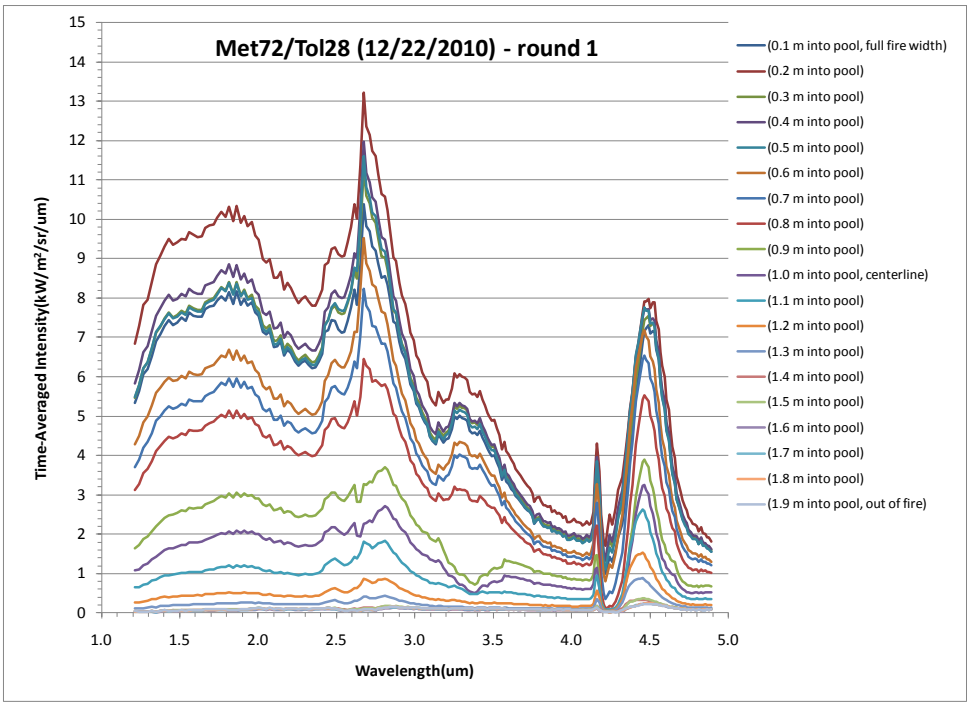

Figure 41 Test 9 Intensity Data – Round 1.

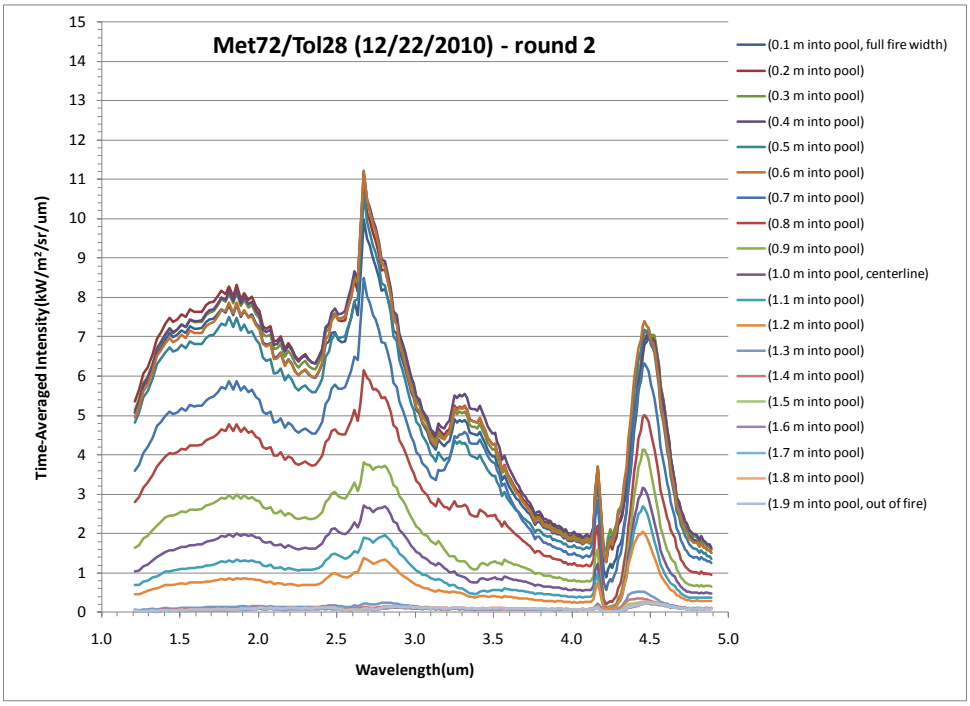

Figure 42 Test 9 Intensity Data – Round 2.

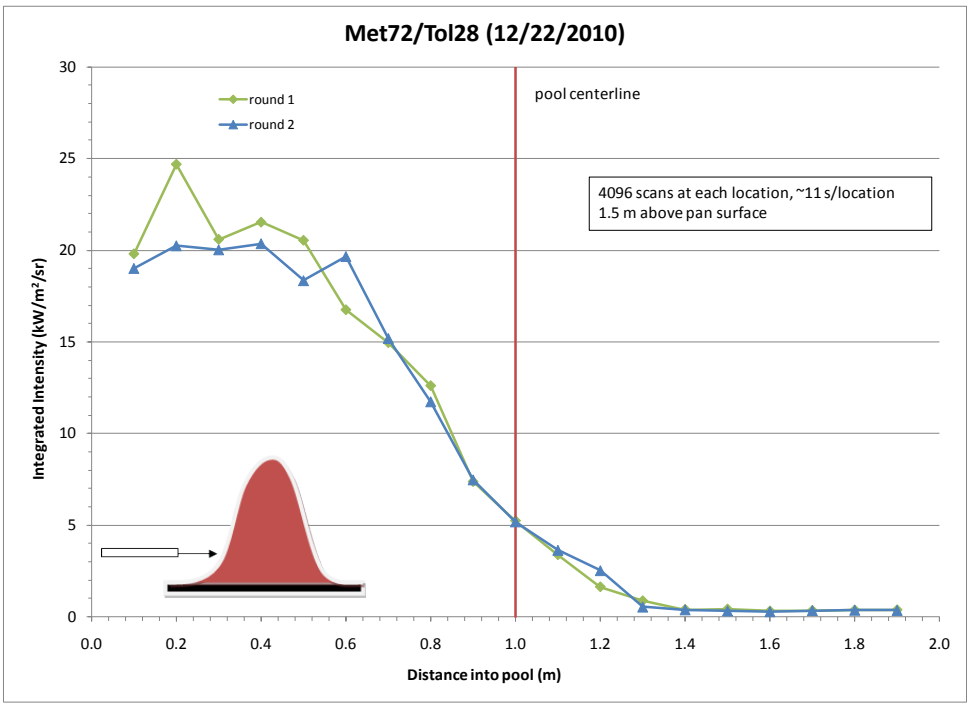

Figure 43 Test 9 Integrated Intensity Data.

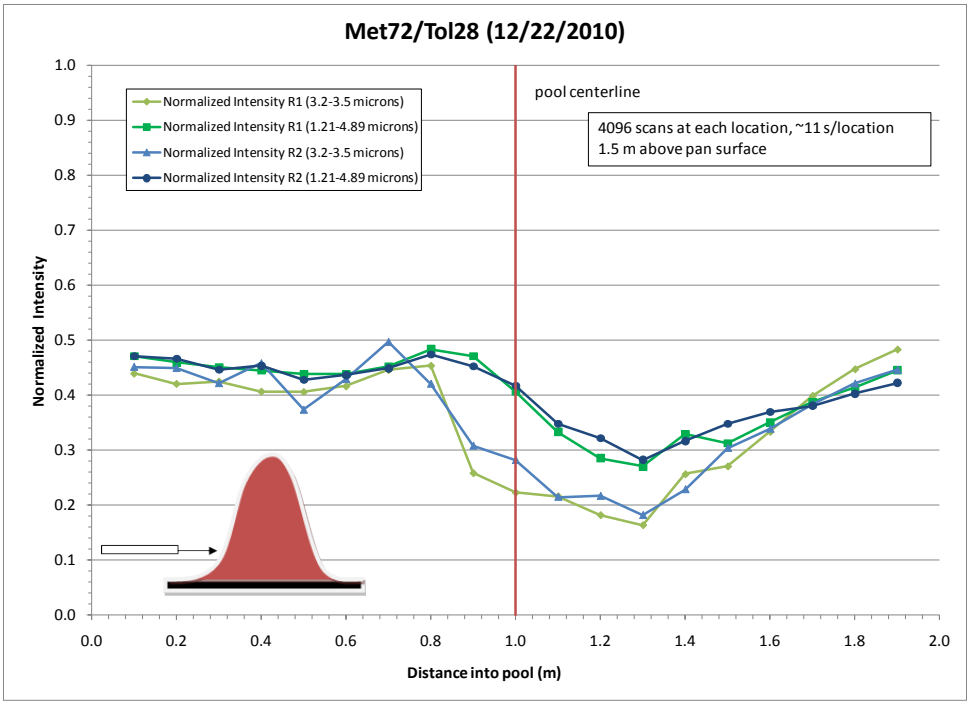

Figure 44 Test 9 Normalized Intensity Data.

6. INTENSITY MEASUREMNT DISCUSSION

Plots are provided for all tests (grouped by the two fuel mixtures) showing the integrated intensity and the normalized intensity over two wavelengths, the full spectrometer wavelength (1.2-4.9 microns) and between 3.2-3.5 microns. In addition, the fire profile is shown giving the left and right edge of the fire for each fuel mixture. In all plots the spectrometer was moved from right (1 m location) to left (-1 m location).

The data show two points of interest. First, the fires for both fuel mixtures are not optically thick, as there was a reduction in integrated intensity at each location as the spectrometer was translated into the fire.

Second, normalizing each spectrum by its maximum value showed that there was proportionately less energy in certain bands within the central region of the fire – possibly indicating unreacted fuel as would be found in the vapor dome.

There was a significant absorption band centered at about 3.4 microns (covering the range of about 3.2 microns to about 3.5 microns) that is likely caused by the C-H bond stretching [Suo-Anttila et al 2009]. It is believed that energy in this band is absorbed in the C-H bonds, resulting in non-black absorption.

The data show almost zero radiation from 3.2 to 3.5 microns for spectra recorded near the center of the fire at the 0.5 m scan height, and the radiation tended to increase as the scan height increased. The emission in this portion of the spectrum also increased as the spectrometer was moved away from the center of the fire plume. A review of the average (normalized) emission in the 3.2 to 3.5 micron bands against distance into the pool show an approximate constant baseline level for probe locations of ~0.2-0.4 m for the azeotrope mixture and ~0.2 m for the Methanol90%/Toluene10% mixture, then followed by a dip in the radiation as the spectrometer viewed near the centerline of the fire. This dip might provide an indication of the lateral extent of the vapor dome.

6.1 Methanol 72% / Toluene 28% (Azeotrope) Tests

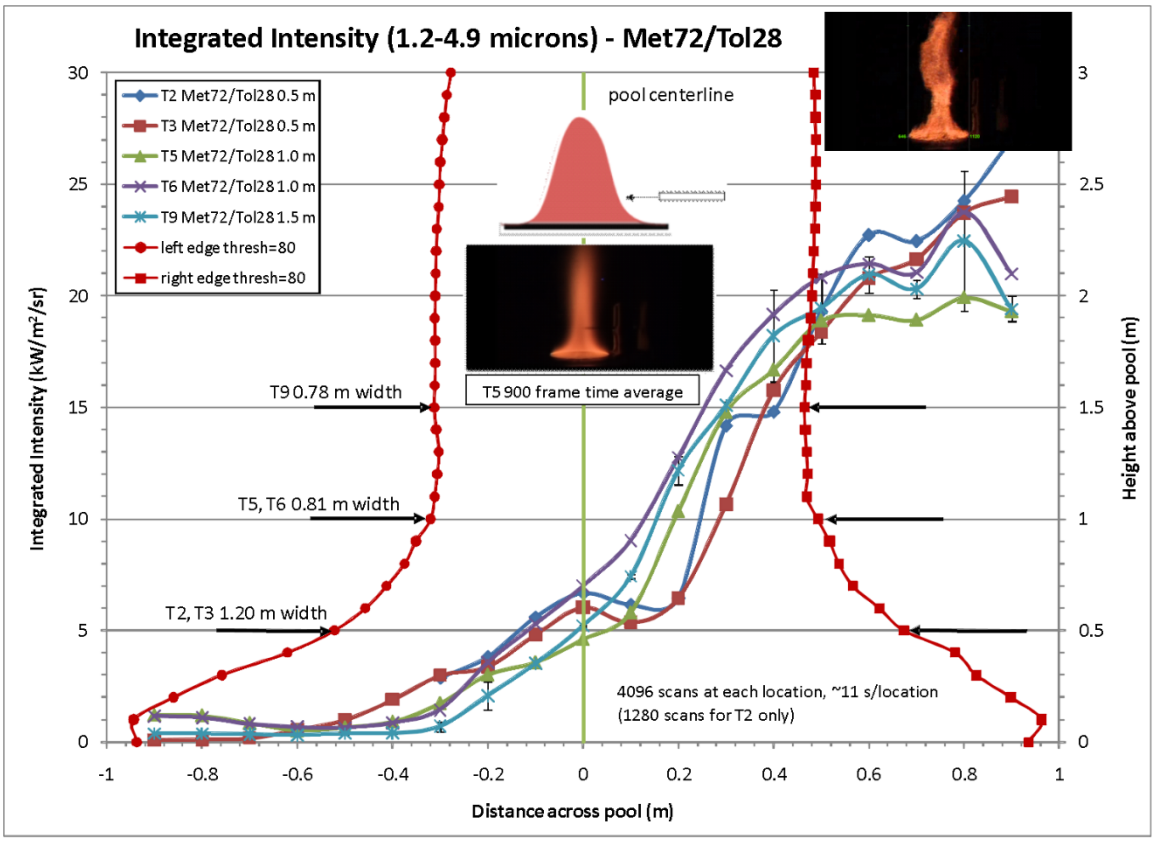

Figure 45 All Met72/Tol28 Tests – Integrated Intensity.

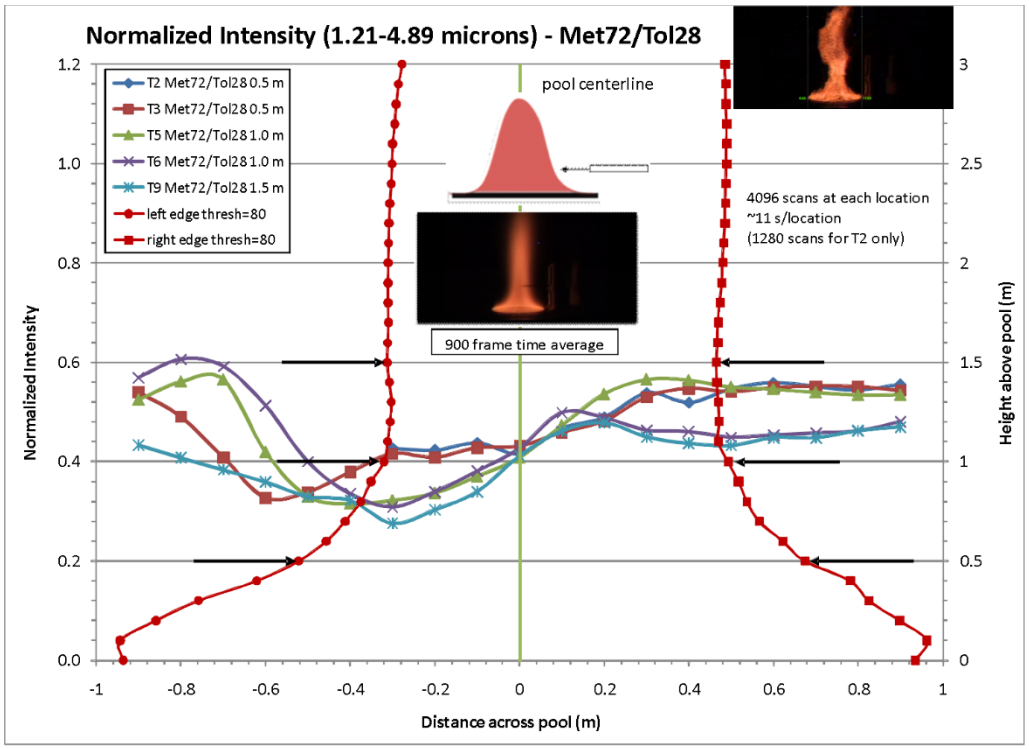

Figure 46 All Met72/Tol28 Tests – Normalized Intensity (1.21-4.89 microns).

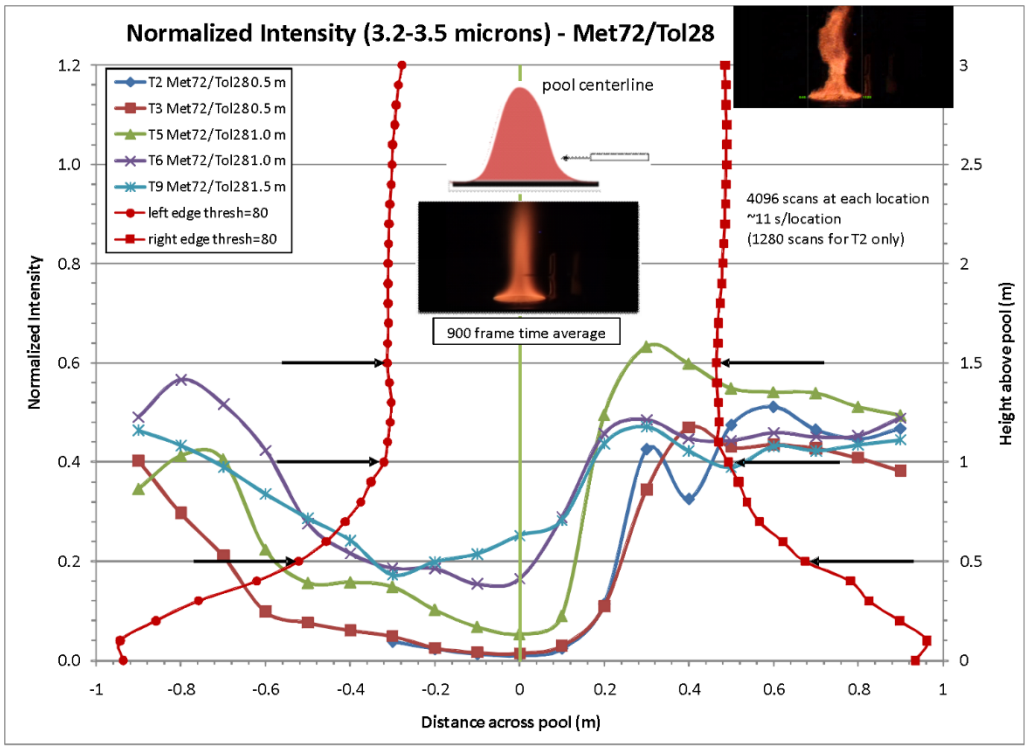

Figure 47 All Met72/Tol28 Tests – Normalized Intensity (3.2-3.5 microns).

6.2 Methanol 90% / Toluene 10% Tests

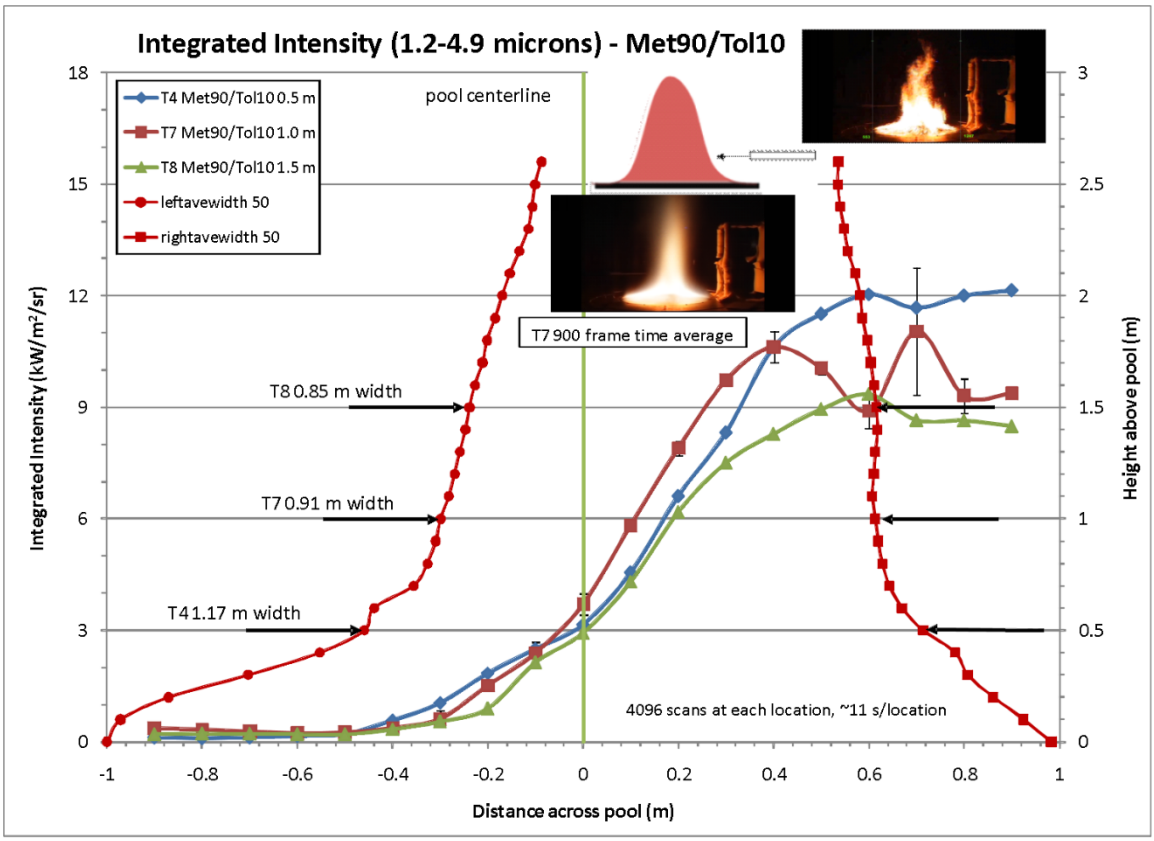

Figure 48 All Met72/Tol28 Tests – Integrated Intensity.

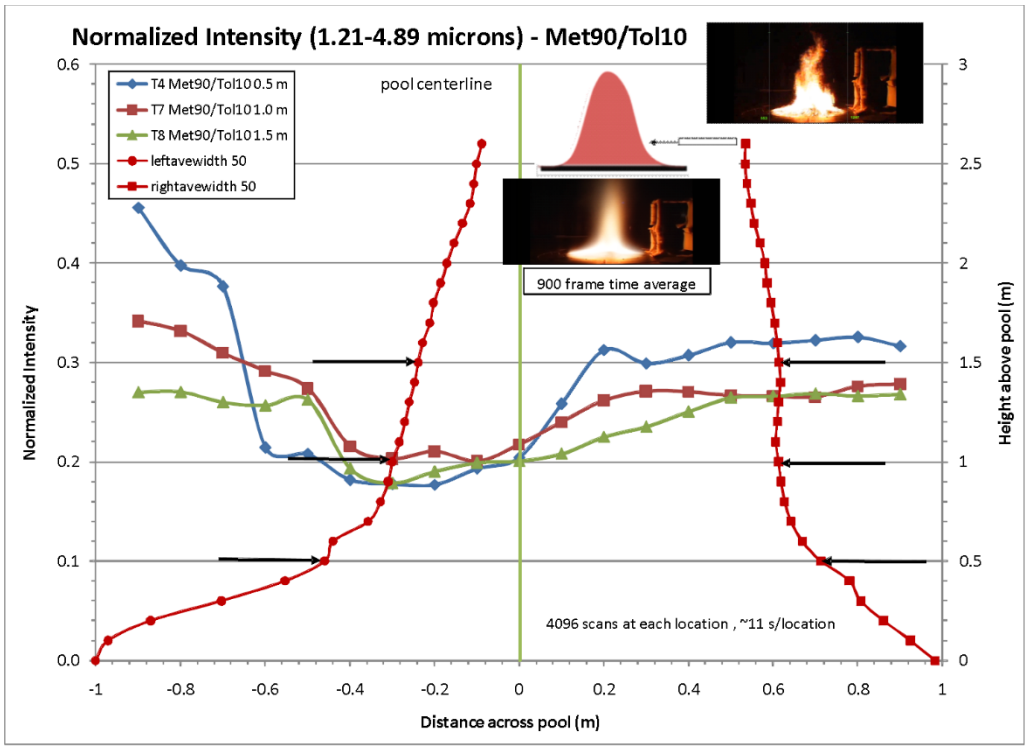

Figure 49 All Met72/Tol28 Tests – Normalized Intensity (1.21-4.89 microns).

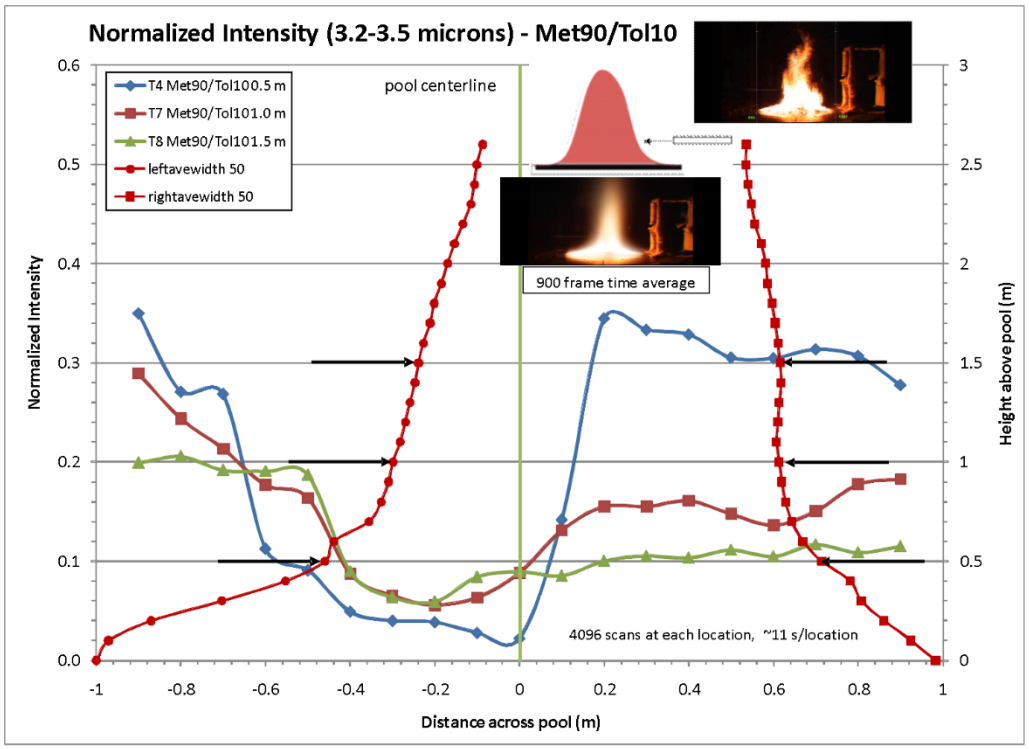

Figure 50 All Met72/Tol28 Tests – Normalized Intensity (3.2-3.5 microns).

7. CONCLUSIONS

A set of experiments and test data are provided in this report that provides radiative intensity data for the validation of models for the radiative transfer equation. The liquid hydrocarbon fuel fire experiments were performed in the fully turbulent scale range (2 m diameter). Two fuel mixtures that provided different soot concentrations were used to ensure viable and compatible data for combined CARS/LII measurements planned to be performed after this series.

Eight experiments were performed, five with an azeotropic fuel mixture (72.4% methanol and 27.6% toluene) and three with a 90% methanol and 10% toluene mixture. For each fuel, intensity measurements (horizontal scans across the fire) were taken at three heights above the fuel surface (0.5 m, 1.0 m, and 1.5 m) and twenty horizontal positions (0.1 m apart). In addition, supplemental measurements of air flow and temperature, fuel temperature and burn rate, and flame surface emissive power, wall heat, and flame height and width provide a complete set on boundary condition data needed for validation of models used in fire simulations.

The reduction in the intensity data appeared to show the presence of the vapor dome, especially at the lower scan heights. This reduction, a significant non-black absorption band centered at about 3.4 microns, is likely caused by the C-H bond stretching.

REFERENCES

Coleman and Steele. *Experimentation and Uncertainty Analysis for Engineers*, Wiley & Sons, 1999.

Kearney, S. P., "Temporally resolved radiation spectra from a sooting, turbulent pool fire," *Proceedings of International Mechanical Engineering Congress and Exposition*, November 11-16, 2001, New York, NY.

Kearney, S., Blanchat, T. K., Ricks, A., Grasser, T., and Jernigan, D., "Test Plan for Validation of the Radiative Transfer Equation," SAND2010-4800, September 2010, Sandia National Laboratories, Albuquerque, NM.

Nakos, J. T., "Uncertainty analysis of thermocouple measurements used in normal and abnormal thermal environment experiments at Sandia's Radiant Heat facility and Lurance Canyon burn site," SAND2004-1023, April 2004, Sandia National Laboratories, Albuquerque, NM.

Nakos, J. T., "Uncertainty analysis of steady state incident heat flux measurements in hydrocarbon fuel fires," SAND2005-7144, December 2005, Sandia National Laboratories, Albuquerque, NM.

Orloff, L., and de Ris, J., "Froude modeling of pool fires*," Proceedings of the 19th Symposium (International) on Combustion*, 1982, pp. 885 – 895.

Romero, V. J., Sherman, M. P., Johnson, J. D., Dempsey, J. F., Edwards, L. R., Chen, K. C., Baron, R. V., and King, C. F., "Development and validation of a component failure model," paper AIAA2005-2141, *46th AIAA/ASME/AHS/ASC Structures, Structural Dynamics, and Materials Conference*, April 18-21, 2005, Austin, TX.

Suo-Anttila, J. M., Blanchat, T. K., Ricks, A. J., Brown, A. L., "Characterization of Thermal Radiation Spectra in 2m Pool Fires," *32nd Symposium (International) on Combustion*, Montreal, Canada, Proceedings of the Combustion Institute, Volume 32, Issue 2, 2009, Pages 2567-2574.

APPENDIX A - ANALYTICAL FRAMEWORK FOR EXPERIMENTAL VALIDATION OF THE RTE IN SIERRA/THERMAL-FLUID DYNAMICS

The goal of this effort is to experimentally validate the form of the radiative transfer equation (RTE) used in Sierra/Thermal-Fluid Dynamics calculations of pool-fire soot radiation. In particular, we wish to assess the validity of key model assumptions, which include: 1) gray soot radiation and 2) the size of the soot particles is much less than the wavelength of the radiation so that scattering is negligible.
We begin by first incorporating assumption #2 above, and neglect the scattering terms in the RTE, which then takes the following form,

$$\frac{dI_\lambda}{ds} = \mu_\lambda I_{\lambda,b}(T) - \mu_\lambda I_\lambda \quad , \tag{1}$$

where I_λ is the radiative intensity at a point, *s,* along the direction of the ray of interest; $I_{\lambda,b}$ is the blackbody spectral intensity at *s,* where the local temperature is T; and μ_λ is the absorption coefficient. Eq. 1 is valid at any instant in time, for any wavelength, λ, at any point along any arbitrary path, *s*. In this context, Eq. 1 simply states that the change in I along s is emission minus absorption. We can integrate Eq. 1 along s to obtain,

$$\int_0^x \frac{dI_\lambda}{ds} ds = \int_0^x \mu_\lambda I_{\lambda,b}(T) ds - \int_0^x \mu_\lambda I_\lambda \, ds \quad , \tag{2a}$$

and perform the trivial integration on the left-hand side to arrive at

$$I_\lambda(x) - I_\lambda(0) = \int_0^x \mu_\lambda I_{\lambda,b}(T) ds - \int_0^x \mu_\lambda I_\lambda \, ds \quad . \tag{2b}$$

$I_\lambda(0) \approx 0$

Here we take the far-field boundary condition at $x = 0$ to be cold surroundings at $T = 300$ K, where I_λ is negligible compared to soot radiation at flame temperatures.

The intent of the measurement program is to test the assumptions used in the RTE for soot radiation only, so we will only consider spectral bands $\Lambda = [(\lambda_1, \lambda_2), (\lambda_3, \lambda_4),...]$ in which soot radiation dominates gas-band radiation, such as in the 1 to 2 μm and/or 3 to 4 μm regions where CO_2 and H_2O are not particularly active. We can then evaluate the terms in Eq. 2b directly on a spectrally resolved basis, or integrate over Λ to test the assumption of gray soot radiation made in SYRINX radiative-transfer calculations.

Framework for a Band-Integrated Test of the Gray Soot Assumption

If we integrate over the soot-radiation bands in Λ, we obtain the following,

$$I_\Lambda(x) = \int_\Lambda I_\lambda(x)d\lambda = \int_\Lambda \int_0^x \mu_\lambda I_{\lambda,b}(T)ds\,d\lambda - \int_\Lambda \int_0^x \mu_\lambda\, I_\lambda\, ds\,d\lambda \quad , \tag{3}$$

where $\int_\Lambda$ indicates an integration over the chosen spectral band or bands. We now examine the spectral dependence of the absorption coefficient, μ_λ, to anticipate the consequences of the gray assumption for soot. The spectral absorption coefficient for soot can be found using the Rayleigh-limit expression for soot extinction in the absence of scattering,

$$\mu_\lambda = \frac{36\pi nk}{\left(n^2-k^2+2\right)^2+4n^2k^2}\frac{f_v}{\lambda} \quad . \tag{4}$$

where f_v is the local soot volume fraction and n and k are the real and imaginary soot refractive indices. Let us first examine the spectrally-integrated absorption coefficient in the first term on the right-hand side of Eq. 3, which has to do with the local emission. Integrating over the wavelength range, with the blackbody intensity as a weighting function, we obtain,

$$\mu_\varepsilon = \frac{\int_\Lambda \mu_\lambda\, I_{\lambda,b}(T)\,d\lambda}{\int_\Lambda I_{\lambda,b}(T)\,d\lambda} \quad . \tag{5}$$

It can be shown[1] that for soot in the small-particle Rayleigh limit the band-integrated absorption coefficient in the emission term takes the form of,

$$\mu_\varepsilon = f(n,k)f_v T \quad , \tag{6}$$

where f is a simple function of the real and imaginary soot refractive indices, n and k, and the bandwidth of the detected radiation.

If we now examine the spectrally-integrated absorption coefficient for the other term on the right-hand side of Eq. 3, which has to do with the local absorption, we obtain

$$\mu_\alpha = \frac{\int_\Lambda \mu_\lambda\, I_\lambda\, d\lambda}{\int_\Lambda I_\lambda\, d\lambda} \quad , \tag{7}$$

[1] M.F. Modest, "Radiative Heat Transfer," McGraw Hill (1993), p. 431.

where the weighting function is now the incident radiation. Calculation of the absorption coefficient for this term therefore requires spectrally-resolved information about the incident radiation flux. When only a spectrally-integrated solution is desired, the gray assumption is usually invoked and the absorption coefficient in the second term is set equal to the absorption coefficient in the first term. This is the assumption invoked in Sierra/Thermal-Fluid Dynamics calculations.

A few observations can be made about Eq. 5 and Eq. 7. If the selected wavelength range is very small, then μ_λ will be relatively constant over Λ and $\mu_\varepsilon \approx \mu_\alpha$ regardless of the differences in the distributions of I_λ and $I_{\lambda,b}(T)$. If I_λ and $I_{\lambda,b}(T)$ have the same wavelength distribution, then $\mu_\varepsilon \approx \mu_\alpha$ as well. However, when there are significant differences in the spectral distributions over a large wavelength range, then $\mu_\varepsilon \neq \mu_\alpha$.

We now make the second key assumption made in the SYRINX calculations (in addition to negligible scattering), which is that the soot radiation is gray. All dependence on λ is then removed and the resulting spectrally integrated coefficients for emission and absorption are equal, $\mu_\varepsilon = \mu_\alpha = \mu$. We further note that,

$$\int_\Lambda I_{\lambda,b}(T)d\lambda = F_\Lambda(T)\frac{\sigma}{\pi}T^4 \quad , \tag{8}$$

where σ is the Stefan-Boltzmann constant, and $F_\Lambda(T)$ is the fraction of the intensity in the Planck spectrum in the bands considered in Λ at temperature T, to obtain,

$$I_\Lambda(x) = \frac{\sigma}{\pi}\int_0^x F_\Lambda(T)\mu T^4 ds - \int_0^x \mu I_\Lambda(s)ds \quad . \tag{9}$$

We can now time average all of the terms in Eq. 9 by the following operations,

$$\overline{I_\Lambda}(x) = \frac{\sigma}{\pi}\frac{1}{\tau}\int_0^\tau \int_0^x F_\Lambda(T)\mu T^4 \, ds\, dt - \frac{1}{\tau}\int_0^\tau \int_0^x \mu I_\Lambda(s)ds \quad , \tag{10}$$

where τ is a sufficiently long time during the steady state burn for the averages computed from experimental data to converge. Now exchange the order of integration and note that $1/\tau \int_0^\tau f(x,t) = \overline{f}(x)$ to get,

$$\overline{I_\Lambda}(x) = \frac{\sigma}{\pi}\int_0^x \overline{F_\Lambda(T)\mu T^4}\, ds - \int_0^x \overline{\mu I_\Lambda}\, ds \quad . \tag{11}$$

We assume that the correlation, $\overline{\mu I_\Lambda}$, between I (a path-integrated quantity) and μ (a locally determined quantity) is weak, so that $\overline{\mu I_\Lambda} = \overline{\mu}\,\overline{I_\Lambda}$. We do not neglect the

$\overline{F_\Lambda(T)\mu T^4}$ correlation. With these assumptions, we arrive at the following expression to formulate a strategy for the planned validation measurements.

$$\overline{I_\Lambda}(x) = \frac{\sigma}{\pi}\int_0^x \overline{F_\Lambda(T)\mu T^4}\, ds - \int_0^x \overline{\mu}\,\overline{I_\Lambda}\, ds \tag{12}$$

Eq. 12 represents an analytical expression to be used as a basis for experiments in which both the assumptions of negligible scattering and gray soot radiation will be tested. To accomplish this, spatial profiles of $\overline{I_\Lambda}(x)$, $\overline{\mu}(x)$, and $\overline{F_\Lambda(T)\mu T^4}$ are required. The diagnostics utilized for each of these measurements are summarized in Table 1 and are discussed in detail elsewhere in this test plan.

It should be noted that while I_Λ and T are measured directly, the absorption coefficient, μ, must be inferred from LII measurements of soot volume fraction, f_v. We then must use appropriate model equations to convert f_v to μ. We will use expressions of the form of Eq. 6 with a variety of literature values for n and k to estimate graybody soot-absorption coefficients for the evaluation of each term in the energy balance of Eq. 12.

Framework for a Spectrally Resolved Test of the RTE in the Absence of Scattering

Since the radiative intensity data inside the fire plume will be spectrally resolved, we can relax the assumption of gray soot behavior and evaluate the RTE using wavelength-specific quantities. Starting from Eq. 2b, we can perform a similar time-averaging process as in Eq. 10, without performing any spectral integration of the RTE. The resulting wavelength-dependent expression,

$$\overline{I_\lambda}(x) = \int_0^x \overline{\mu_\lambda I_{\lambda,b}(T)}\, ds - \int_0^x \overline{\mu_\lambda}\,\overline{I_\lambda}\, ds \quad , \tag{13}$$

where we have, again, assumed weak correlation between μ_λ and I_λ so that $\overline{\mu_\lambda I_\lambda} = \overline{\mu_\lambda}\,\overline{I_\lambda}$. Eq. 13 can be used for validation of the RTE without the assumption of gray soot radiation. As in the case of Eq. 12, we must relate the LII-measured f_v to μ_λ; this can be accomplished using the Rayleigh-limit expression for soot extinction in the absence of scattering (Eq. 4). Eq. 13 can be spectrally integrated to obtain the equivalent of Eq. 12 without the assumption of gray-soot radiation,

$$\overline{I_\Lambda}(x) = \int_\Lambda \int_0^x \overline{\mu_\lambda I_{\lambda,b}(T)}\, ds\, d\lambda - \int_\Lambda \int_0^x \overline{\mu_\lambda}\,\overline{I_\lambda}\, ds\, d\lambda \quad . \tag{14}$$

Comparison of the residuals from Eq. 12 and Eq. 14 provides a partial check of the consistency of the gray soot assumption, especially if the wavelength range is large enough to have a wide variation in the spectral absorption coefficient of soot. If the

residuals are smaller for Eq. 14 than for Eq. 12, then the degree of improvement in the residuals is an indication of the consequence of the gray assumption.

Additional Checks on the Consistency of the Gray Soot Assumption

Additionally, we can compute μ_ε and μ_α from their fundamental definitions using experimentally derived information regarding I_λ and $I_{\lambda,b}(T)$ from the IES and CARS data. The time-averaged absorption coefficient used in the last term on the right-hand side of Eq. 12 is the time-averaged form of Eq. 6,

$$\overline{\mu_\varepsilon} = f(n,k)\overline{f_v T} \quad . \tag{15}$$

This absorption coefficient is actually based upon the emission term (the first term on the right-hand side of Eq. 12), and is applied everywhere when the gray assumption is invoked. If the gray assumption is not invoked, the spectrally-integrated and time-averaged absorption coefficient for the same term can be approximated as

$$\overline{\mu_\alpha} = \frac{\int_\Lambda \overline{\mu_\lambda}\,\overline{I_\lambda}\, d\lambda}{\overline{I_\Lambda}} \quad . \tag{16}$$

This approximation cannot be justified when time-averaging Eq. 7, but it is useful in the present context because it can be thought of as the absorption coefficient that makes the second term on the right-hand side of Eq. 12 equivalent to the second term on the right-hand side of Eq. 14. Using IES measurements of I_λ, CARS temperature measurements for calculation of $I_{\lambda,b}(T)$ and LII-determined soot f_v in conjunction with Eq. 4 for calculation of μ_λ, $\overline{\mu_\varepsilon}$ and $\overline{\mu_\alpha}$ can be calculated at selected points along the path. The agreement of $\overline{\mu_\varepsilon}$ and $\overline{\mu_\alpha}$ to each other can be used as a validation of the gray soot assumption that does not depend upon the results of Eq. 12, and the differences between $\overline{\mu_\varepsilon}$ and $\overline{\mu_\alpha}$ may help to explain differences in the residuals of Eq. 12 and Eq. 14.

In the preceding discussion it has been assumed that the only spectral bands being considered are bands in which gas-phase species do not contribute significantly. This is necessary when validating the solution of the RTE using the residuals of Eqs. 12 through 14, where gas-band contributions cannot be accounted for. The RTE cannot be fully evaluated in bands in which the gases participate strongly, but the energy absorbed and emitted by soot can still be assessed. The energy absorbed and emitted by soot in these bands is relevant to the question of the degree to which soot actually behaves as a gray body in a fire, so this question is best addressed by comparing $\overline{\mu_\varepsilon}$ to $\overline{\mu_\alpha}$ when integrated over the entire range of the IES measurements.

Summary of Measurement Approaches for RTE Validation

Each of the three terms in Eqs. 12 and 14 will be determined by sampling I_Λ, μ, and T in a pointwise fashion for 30-40 minutes. The I_Λ measurements will be performed using a separate diagnostic than for the μ/T data, so that these results will not be correlated. The μ/T data will be recorded simultaneously, and should be statistically correlated for a measurement of the $\overline{\mu T^4}$ term in the turbulent pool-fire environment. We anticipate 10^4 statistically independent (not time correlated) samples to be obtained for calculation of the time-mean in Eq. 6. These integrals in Eq. 6 will be numerically evaluated using data from 8-10 x locations along the line of sight. The measurement techniques to be employed are summarized in Table 1; the details of these diagnostic approaches can be found later in this test plan.

Table 6 List of Optical Combustion Diagnostics for RTE Validation Measurements

QUANTITY	MEASUREMENT APPROACH
Temperature, T	Coherent anti-Stokes Raman scattering (CARS)
Absorption coefficient, μ	Laser-induced incandescence (LII) measurements of soot f_v **combined with soot refractive index and model to convert f_v to μ**
Radiation Intensity, I_Λ	Infrared emission spectroscopy (IES) limited to soot-dominated radiation bands
Emission term, $\overline{\mu T^4}$	Simultaneous CARS and LII temperature and soot f_v

DISTRIBUTION

1	MS0384	J. E. Johannes	1500
1	MS0747	A. J. Ricks	6223
1	MS0826	S. P. Kearney	1512
1	MS0836	J. C. Hewson	1532
1	MS0836	S. P. Domino	1541
1	MS1135	R. D. Watkins	1533
1	MS1135	T. K. Blanchat	1532
1	MS1135	A. Luketa	1532
1	MS1135	D. A. Jernigan	1533
1	MS1139	D. M. Cotter	1530
1	MS0899	Technical Library (electronic copy)	9536


Sandia National Laboratories